Z-Band: On-world Interactions Using Wrist-based Electrical Impedance Sensing

ANANDGHAN WAGHMARE*, Paul G. Allen School of Computer Science & Engineering, University of Washington, USA
SANJAY VARGHESE, University of Washington, USA
ZHIHAN ZHANG, Paul G. Allen School of Computer Science & Engineering, University of Washington, USA
ISHAN CHATTERJEE, Paul G. Allen School of Computer Science & Engineering, University of Washington, USA
RITESH TEKRIWAL, University of Washington, USA
SHWETAK PATEL, Paul G. Allen School of Computer Science & Engineering, University of Washington, USA

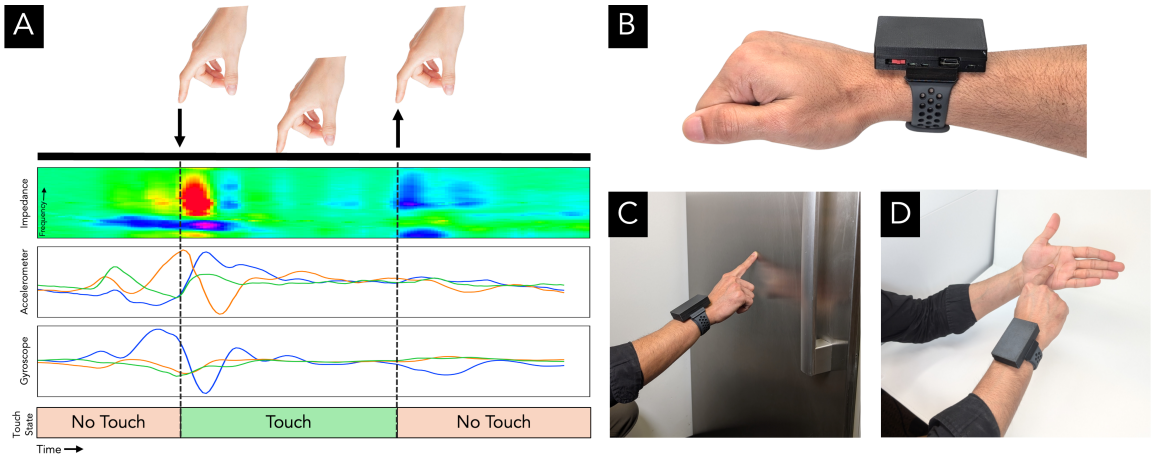


Fig. 1. (A) Figure showing raw RF and IMU signal data from the Z-Band prototype, highlighting the exact moments when touch begins and ends, and demonstrating the system's stateful touch detection capability. (B) The Z-Band-Lite prototype device worn by a user. Examples of surfaces on which Z-Band can be used, such as (C) a refrigerator door or (D) the palm of the other hand.

*Corresponding author.

Authors' Contact Information: Anandghan Waghmare, Paul G. Allen School of Computer Science & Engineering, University of Washington, USA, anandw@cs.washington.edu; Sanjay Varghese, University of Washington, USA, snjy1697@uw.edu; Zhihan Zhang, Paul G. Allen School of Computer Science & Engineering, University of Washington, USA, zzhihan@cs.washington.edu; Ishan Chatterjee, Paul G. Allen School of Computer Science & Engineering, University of Washington, USA, ichat@cs.washington.edu; Ritesh Tekriwal, University of Washington, USA, rtekri@uw.edu; Shwetak Patel, Paul G. Allen School of Computer Science & Engineering, University of Washington, USA, shwetak@cs.washington.edu.

This work is licensed under a Creative Commons Attribution-NonCommercial-ShareAlike 4.0 International License.
© 2025 Copyright held by the owner/author(s).
ACM 2474-9567/2025/12-ART216
https://doi.org/10.1145/3770637

We introduce Z-Band, a wearable device that fuses bio-impedance and inertial sensing to enable robust stateful touch detection on various everyday, non-instrumented surfaces. Stateful touch detection, achieved by injecting wide-band, swept-frequency RF signals through the wrist and analyzing their reflections and transmissions, facilitates sensitive touch detection even on challenging dielectric surfaces. We build upon this foundation to support a range of gestures, including swipes and taps, and enable touch pressure sensing. User studies demonstrate over 95% touch detection accuracy in stationary scenarios and over 90% in motion without requiring per-user calibration. This approach offers a seamless, natural way to interact with wearables and receive haptic feedback through touch gestures on any surface, making possible a new generation of interactive experiences.

CCS Concepts: • **Human-centered computing → Interaction devices**; **Ubiquitous and mobile devices**; **Interaction techniques**.

Additional Key Words and Phrases: Wearable input devices, AR/VR, RF sensing, Sensor fusion, Machine Learning, Interaction Techniques

ACM Reference Format:
Anandghan Waghmare, Sanjay Varghese, Zhihan Zhang, Ishan Chatterjee, Ritesh Tekriwal, and Shwetak Patel. 2025. Z-Band: On-world Interactions Using Wrist-based Electrical Impedance Sensing. *Proc. ACM Interact. Mob. Wearable Ubiquitous Technol.* 9, 4, Article 216 (December 2025), 45 pages. https://doi.org/10.1145/3770637

1 INTRODUCTION

Modern touchscreens and trackpads make touch interactions a pillar of modern HCI interaction paradigms. By offering valuable haptic feedback and closed-loop control, surface interactions like taps and swipes can be quick and ergonomic [31]. However, robustly sensing these interactions often requires instrumenting the surface, confining interaction to the touch-sensitive space [8, 17, 56].

To enable "touch anywhere" for applications like mobile or XR device control, researchers have explored wearable techniques for touch. Though promising, these solutions face limitations. Vision-based methods, commonly leveraged in AR/VR for tracking user's hands, require a direct line of sight, are susceptible to occlusion, and struggle with the "last centimeter problem," making precise touch timing difficult [29, 52, 55]. Other systems require mounting the camera in close proximity to the point of interaction, such as the fingertip or pad, compromising ergonomics [41, 53]. Non-line-of-sight methods typically remain restricted to non-stateful interactions like quick taps [13, 35]. However, accurately detecting the exact start and end of touch events unlocks a realm of stateful interactions, like dragging and dropping and continuous input, significantly enriching the user experience [3, 15].

Additionally, while existing wearable systems have demonstrated surface interaction in stationary scenarios [13, 25, 35], enabling seamless interaction in mobile settings remains a challenge. In mobile scenarios, sensor data from sources like inertial measurement units (IMUs) and bio-acoustic methods becomes noisy due to motion artifacts, diminishing accuracy [20].

In response to these limitations, we propose *Z-Band, a wrist-worn wearable device that can detect stateful touch interactions on external, noninstrumented surfaces without requiring a line-of-sight.* To power its capabilities, Z-Band employs electrical impedance sensing fused with IMU signals. Our system enables surface interaction across a broader range of materials, including soft materials like cloth or skin, where IMU-only systems struggle due to the minimal signal variations they produce in IMU data [42]. Our RF (Radio Frequency)+IMU hybrid system enhances sensitivity, allowing accurate surface interaction detection even on soft materials. Additionally, Z-Band performs consistently in dynamic scenarios like walking and uniquely provides the ability to detect touch pressure, further enhancing its functionality.

We combine RF and IMU sensing in Z-Band to leverage their complementary strengths and mitigate their individual limitations. RF impedance sensing offers stable, stateful touch detection, especially in low-motion contexts, but its sensitivity can be affected by electrode placement and environmental noise. Conversely, IMU accurately captures motion-rich contexts. However, it struggles with static or low-motion interactions (e.g.,

touch-and-hold) and is prone to false positives during mobile usage due to body movement. By fusing these RF and IMU modalities, we achieve robust performance across both stationary and dynamic scenarios: RF anchors the system in detecting precise contact events, while IMU disambiguates intent and additionally enriches interaction types such as swipes. Our evaluation (Section 8.2.5) shows that sensor fusion significantly improves touch detection performance.

Z-Band utilizes high-frequency radio signals from 1 MHz to 1000 MHz injected at the wrist for sensing touch interactions. These signals propagate efficiently along the skin's surface, reaching the fingers, and are modulated by interactions with external surfaces, enabling recognition of external touch events. The choice of high-frequency signals is critical to the system's effectiveness since it ensures farther propagation along the hand. Lower-frequency signals (kHz to low MHz) penetrate deeper into biological tissues due to their longer wavelengths [40], making them suitable for probing interior body structure for applications like electrical impedance tomography (EIT) and muscle activity monitoring [33]; however, they also experience higher resistive losses, which can limit their propagation distance along the body's surface and limit their suitability for sensing at the fingers [61]. In contrast, higher-frequency signals interact primarily with the skin's outer layers, minimizing deep penetration while traveling along the body's surface [10]. This effect allows the signals to travel from the wrist to the fingers, where finger interactions cause measurable variations, enabling touch detection from the wrist.

For electrical impedance sensing, Z-Band uses a low-cost, portable vector network analyzer ([22, 47, 48]) to inject radio frequency (RF) waves at the wrist. *Importantly, our RF system can detect subtle touches even on challenging dielectric materials, such as plastic or wood, which exhibit lower signal variation compared to conductive materials due to their limited influence on RF propagation and weaker capacitive coupling.* We achieve this enhanced touch sensitivity in two ways. First, we conduct a wide-band frequency sweep of high frequencies (1-1000 MHz), which are particularly responsive to hand interactions given their short wavelength [34]. Second, we design custom front-end architectures for the VNA to boost the signal-to-noise ratio for sensing at the wrist, even when the interaction site—the fingertips—is further away. *This highly sensitive signal also enables Z-Band to detect touch pressure, adding an extra layer of richness to the interactions.* By hybridizing electrical impedance sensing with inertial sensing, Z-Band enriches robustness to touch segmentation and captures hand motion, facilitating interactions like swipes and taps.

In this remainder of this paper, we first explain the theory and functions of impedance sensing. We then conduct multiple simulations across various scenarios to demonstrate the feasibility of this sensing approach and to computationally optimize our sensing parameters. Next, we present three front-end architecture design prototypes and discuss the results, trade-offs, and design choices we made for the Z-Band. Finally, we conduct a user study to evaluate the system, demonstrating its robustness in touch detection and showcasing its effectiveness in gesture recognition.

This work makes the following contributions:

- Z-Band, a new wristband system that enables stateful touch segmentation across diverse materials and mobile scenarios while detecting touch pressure—without requiring line-of-sight sensors or surface instrumentation.
- A comprehensive examination of wrist-based, high-frequency impedance sensing, encompassing electromagnetic (EM) propagation simulations, three distinct RF architecture designs, and comparative analysis to guide optimal design choices.
- A hardware and software pipeline, rigorously evaluated through user studies, that demonstrates the effectiveness of this technique for touch segmentation across diverse scenarios and its efficacy in facilitating on-world interactions.

2 RELATED WORK

Touch interaction is foundational to human–computer interaction. Though traditional touchscreens offer robust capabilities, they are limited to predefined surfaces. A growing body of work has explored enabling surface interactions beyond static touchscreens, such as on desks, walls, or even the user's own body. However, current systems often make trade-offs in portability, surface compatibility, or interaction expressiveness. Many require bulky setups, depend on line-of-sight, or fail to segment touch events reliably—especially in low-motion or mobile contexts. These limitations hinder real-world deployment in scenarios where touch can occur spontaneously, across diverse surfaces, and without constrained environments.

In this section, we review existing approaches to surface interaction, focusing on their sensing modalities, limitations in interaction fidelity, and constraints in practical usability. We then position our method, Z-Band, as a solution that addresses critical gaps in prior work by *enabling accurate, stateful touch segmentation on diverse surfaces from a minimal wrist-mounted form factor, even under mobile conditions.*

2.1 Sensing Techniques for Surface Interactions

Traditional surface interaction sensing typically relies on instrumented surfaces integrated with sensors. Researchers have implemented a wide array of on-surface sensor modalities to enable interaction on various scales, from device-specific implementations to larger, whole-room setups. For instance, acoustic[16, 18], capacitive [39] and vibration [9] sensing target small interaction spaces, such as furniture or device surfaces, by using mounted contact microphones, capacitive, or piezo vibration sensors. Wall++ [58] and GravitySpace [1] extend the sensing space to large-scale surfaces like walls and floors for whole-room input detection utilizing capacitive and optical sensors, respectively. They are confined to predefined instrumented areas or require direct line-of-sight-limiting, cross-surface switching capabilities.

Wearable sensing approaches have sought to circumvent the constraints of static, instrumented surfaces. Acoustic methods, including Skinput [17], ViBand [28], Acustico [13], and SoundScroll [25], leverage body-mounted sensors to detect touch events through vibrations and sound waves. However, these systems often struggle with accurately segmenting touch states, such as touch down and touch up, particularly in scenarios where parts of the interaction lack dynamic motion since detection relies solely on movement.

Inertial-based systems, for example, TapID [35], [15], use wrist-mounted IMUs to detect taps on noninstrumented surfaces but cannot determine touch states, limiting interactions like drag-and-drop. The performance of such systems across dynamic scenarios with body motion (where motion adds noise to IMU data) [20]or on varied surfaces remains unexplored since evaluation has been limited to seated contexts and a single hard surface. Shi et al. [41] use nail-mounted IMUs to detect touch gestures, providing stateful interaction capabilities but requiring direct attachment to the user's fingers.

Vision-based approaches, including RGB [30, 51, 52] and thermal cameras [29], can detect touch interactions on surfaces. Though these systems can support interaction on arbitrary surfaces, such as in Niikura et al. [37], they highly depend on environmental conditions and require an unobstructed line-of-sight—factors that limit their reliability in real-world, everyday scenarios.

These limitations highlight the need for a modality that is inherently body-centric, in a convenient form factor, and resilient to environmental variability. To that end, we explore electrical sensing approaches, which offer unique advantages in detecting contact events through the body's intrinsic properties.

2.2 Electrical Sensing for HCI

Touchscreens have long been the gold standard for precise touch segmentation, utilizing mutual or self-capacitance techniques to detect touch gestures with high accuracy. By distributing multiple electrodes across the surface,

continuous tracking of finger movements is achieved [8]. Electrick [56] and Touché [39] measure contact and grasp styles on conductive objects, but these systems are inherently limited to predefined surfaces.

Recent advances in wearable electrical sensing have expanded the possibilities for surface interactions beyond fixed locations. Electromyography (EMG) systems, such as Saponsas et al. [38], Meta CTRL-labs [7], and others [32, 49], use between eight and 64 electrodes placed around the forearm or wrist to measure muscle activity and infer hand gestures. However, though EMG is effective for recognizing gestures, it is less suited for detecting touch contact with surfaces, making impedance sensing a more suitable alternative for this purpose.

Electrical impedance tomography (EIT) offers a method for sensing across the body using multiple electrodes (>=8) to map conductivity changes in the hand and forearm. Systems like Tomo [54, 57] and EIT-Kit series [27, 62] demonstrate EIT's utility for pose recognition, yet these setups often involve complex instrumentation that may be unsuitable for everyday use. Over-air impedance systems, such as Etherpose [22] and Pantoenna [23], explore non- contact impedance characteristic sensing methods for pose estimation. Though these systems avoid the physical constraints of EIT, they require large antennae to operate effectively at the frequencies necessary for over-air impedance sensing.

More closely related to our work are systems that utilize the body as a waveguide for electrical signals, enabling robust touch segmentation since the contact modulates the transmission properties. Studies such as BodyRC [50] and ActiTouch [55] use electrodes at different body points to detect touch events, leveraging the body's natural electrical properties. ElectroRing [21] refines this concept by using a single point of instrumentation on the finger for pinch segmentation. However, these systems are often limited to certain surfaces or specific gestures, highlighting the need for broader material compatibility.

Although these body-conducted electrical systems demonstrate the feasibility of detecting touch via the body's natural electrical transmission properties, they still fall short in key aspects: compatibility with non-conductive materials, form factor constraints, and limitations in segmentation fidelity. Notably, no prior system achieves accurate, continuous touch-state detection from a wrist-worn device across common real-world materials like wood, glass, and skin. Further, the challenge of signal attenuation from the wrist to the fingers remains largely unaddressed, stalling progress toward smartwatch-scale interaction systems. This motivates the core contribution of Z-Band.

Most similar to our sensing method is Z-Ring[47, 60], which uses wide-band RF sensing to detect hand interactions, including touch on external surfaces; however, it has been demonstrated only for conductive surfaces. Moving this capability to a wrist-based form introduces significant challenges—notably, a drastic reduction in signal strength due to increased distance from the interaction site and the need to function reliably on non-conductive surfaces. The signal-to-noise ratio (SNR) decreases significantly as the sensing site (wrist) moves farther from the interaction site (fingers). For example, as measured by a commercial VNA, using a signal electrode at the base of the index finger yields a signal change of 0.23 dB when touching a grounded metallic surface. Touching the same surface with the same electrode at the wrist yields a signal change of only 0.04 dB. For surfaces like wood, this signal change is 0.06 dB for an electrode at the finger base and 0.02 dB for the wrist. When sensing from the wrist, the reduction in signal change occurs because the signal undergoes greater attenuation due to the longer transmission path through the body between the wrist and fingers. Our work directly tackles these challenges by (1) using a custom RF front-end that amplifies signal strength and (2) by fusing IMU data to enhance segmentation reliability under mobility and low-SNR conditions.

Z-Band surpasses these previous RF systems in two ways. First, it incorporates a *custom analog front-end, computationally optimized electrode design, and integration with inertial sensing*. It thus exhibits higher sensitivity and enables a convenient wrist-based setup with only two electrodes, making it compatible with the current smartwatch form factor. Second, Z-Band achieves *accurate and stateful touch segmentation not only on conductive surfaces but also on low-permittivity materials*, such as wood, plastic, glass, and skin. To provide additional context

to touch interactions, our system can sense touch pressure and utilize IMU data to capture motion during touch, building rich interactions, such as swipes, on top of our fundamental touch segmentation.

Table 1 compares the state of prior wearable systems across multiple sensing dimensions. Though several approaches support aspects of stateful touch or mobile use, few combine these capabilities with compatibility across diverse surfaces in a convenient form factor. Z-Band unifies these elements, offering a promising step toward more practical and scalable touch interaction in everyday settings.

Table 1. Comparison of representative wearable touch interaction systems across sensing modality, surface compatibility, and study conditions.

Work	Sensing Modality	Interaction Type	Interaction Surfaces	Form Factor	Touch Pressure	Study Conditions
TapID [35]	IMU	● Non-Stateful	● Rigid Surfaces	● Wristband	● No	Sitting
Ready Set Touch! [41]	IMU	● Stateful Touch	● Diverse Surfaces	● Nail-mounted	● No	Sitting + Walking
SoundScroll [25]	Acoustic	● Stateful Touch (active movement)	● Diverse Surfaces	● Wristband	● No	Sitting
Acustico [13]	IMU + Acoustic	● Non-Stateful	● Rigid Surfaces	● Wristband (requires contact)	● No	Sitting
Anywhere Surface Touch [37]	Camera + Acoustic	● Stateful Touch	● Diverse Surfaces	● Wristband	● No	Sitting
ShadowTouch [30]	Camera	● Stateful Touch	● Rigid Surfaces	● Wristband + Head-mounted (LOS)	● No	Sitting
EgoTouch [36]	Camera	● Stateful Touch	● On-body	● Head-mounted (LOS)	● Yes	Sitting + Walking
SkinTrack [59]	Electromagnetic	● Stateful Touch	● On-body	● Wristband + Ring	● No	Sitting
Electroring [21]	Electrical	● Stateful Touch	● On-body	● Ring	● Not Explored	Sitting
Z-Ring [47]	Bio-impedance	● Stateful Touch	● On-body + External Conductive Surfaces	● Ring	● Not Explored	Sitting
Z-Band (this work)	**Bio-impedance**	**● Stateful Touch**	**● Diverse Surfaces**	**● Wristband**	**● Yes**	**Sitting + Walking**

3 ELECTRICAL IMPEDANCE SENSING

Electrical impedance sensing can capture subtle changes in the human body caused by movement or environmental interactions by detecting and characterizing various physiological parameters. We now present the operational principles of electrical impedance sensing, particularly in the context of human-computer interaction (HCI).

3.1 General Sensing Principles

Electrical impedance sensing works by applying an alternating current (AC) signal to the body and measuring how biological structures affect its propagation. The opposition to current flow is characterized by *impedance* (Z), which comprises two fundamental components: *resistance* (R) and *reactance* (X). Resistance represents the real part of impedance and quantifies energy dissipation as heat during current flow through tissues. Reactance represents the imaginary part and arises from energy storage in capacitive and inductive elements within the tissue. In biological systems, capacitive reactance dominates due to cell membranes acting as dielectric barriers that temporarily store charge. The complex impedance is expressed as:

$$Z = R + jX \tag{1}$$

where j is the imaginary unit ($j = \sqrt{-1}$) distinguishing between resistive (energy dissipation) and reactive (energy storage) components.

The frequency-dependent behavior of electrical signals in biological tissues is governed by the interplay between capacitive reactance and the impedance characteristics of the electrode-tissue interface. The capacitive reactance (X_C) of biological structures, primarily determined by cell membrane capacitance, follows:

$$X_C = \frac{1}{2\pi f C} \tag{2}$$

where f is the signal frequency and C is the capacitance. At low frequencies, X_C is large, causing cell membranes to act as significant barriers that impede transmembrane current flow. Consequently, current predominantly follows extracellular pathways around cells, where ionic conduction through interstitial fluids offers lower impedance. As frequency increases, X_C decreases, progressively reducing the membrane's blocking effect. At sufficiently high frequencies, current can penetrate cell membranes more readily, enabling current flow through both intracellular and extracellular compartments. This frequency-dependent transition is the basis for bioimpedance spectroscopy techniques that probe tissue composition.

The penetration depth of electrical signals is also influenced by the impedance mismatch at the electrode-skin interface. The power reflection coefficient (Γ) at this boundary is given by:

$$\Gamma = \left| \frac{Z_{\text{skin}} - Z_{\text{electrode}}}{Z_{\text{skin}} + Z_{\text{electrode}}} \right|^2 \tag{3}$$

where $Z_{\text{electrode}}$ is the electrode impedance and Z_{skin} is the skin impedance. Skin impedance decreases with increasing frequency due to the reduced capacitive reactance of the stratum corneum (the outermost skin layer, which has high capacitance). At low frequencies, the large Z_{skin} creates a smaller impedance mismatch with the electrode, resulting in lower reflection and greater signal transmission into deeper tissues. At high frequencies, Z_{skin} decreases substantially while $Z_{\text{electrode}}$ remains relatively constant, increasing the impedance mismatch and causing greater reflection at the interface. Additionally, high-frequency signals experience the skin effect, where current density concentrates near the surface due to self-inductance and the tendency of alternating currents to flow along paths of least impedance near conductor surfaces.

Therefore, *low-frequency signals penetrate deeper into tissues* because high membrane reactance confines current to extracellular pathways, while low electrode-skin reflection allows effective coupling into the body. These characteristics make low-frequency impedance measurements suitable for applications such as body composition analysis and deep tissue monitoring. Conversely, *high-frequency signals remain more confined to superficial layers* due to reduced skin impedance causing greater electrode-skin reflection, combined with the skin effect. This behavior makes high-frequency sensing ideal for surface applications such as touch detection and skin impedance measurements.

3.2 Impedance Measurement Setup

In our setup, we galvanically inject a sweep of RF signals into the body (at the wrist), allowing it to act as an electrical waveguide [14, 63]. These signals propagate through the hand and interact with the contacted materials.

Figure 2a shows the equivalent circuit model for impedance measurement, showing signal source, electrode impedance, hand impedance, and surface impedance. The total impedance of the system, as seen by the signal source, can be expressed as:

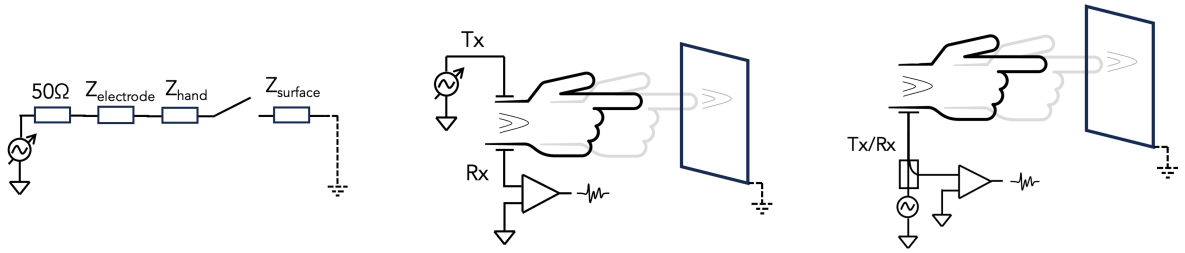
$$Z_{\text{total}} = 50\ \Omega + Z_{\text{electrode}} + Z_{\text{hand}} + Z_{\text{surface}}. \tag{4}$$

At impedance transitions, such as at the hand-material interface, part of the signal is reflected, while the rest is either dissipated within the hand or transmitted into the material. This behavior is influenced by the material's

permittivity, which defines how easily it can store and transmit electric fields. Higher-permittivity materials, such as water or conductive surfaces, allow more signal transmission and absorption, while lower-permittivity materials, like plastic or wood, cause greater reflection and reduced signal penetration. The interaction between the injected signal and the contacted material modulates the overall impedance profile Z_{total}, allowing touch contact to be inferred based on changes in the reflected and transmitted signals.

To capture these variations, we measure the reflected signal either at a secondary electrode (Figure 2b) or at the injection site (Figure 2c). By analyzing these signals, we can characterize the hand's role as a waveguide and quantify the impedance change introduced by different materials. The ability to detect changes in wave propagation due to material contact enables robust touch sensing without requiring direct instrumentation of the surface.

However, wave behavior is influenced not only by material contact but also by several other factors, including signal frequency and electrode geometry [2]. These factors can introduce variability in impedance measurements, necessitating a deeper understanding of their effects. To address this, we conduct comprehensive simulations to analyze how these parameters impact signal changes in Section 4. By identifying distinct impedance variations associated with material interactions while mitigating confounding effects, we aim to optimize sensing robustness and enhance the reliability of Z-Band's touch detection system.



(a) The equivalent circuit model represents the total impedance pathway, including the signal source, electrode, hand, and contacted surface.

(b) S_{21}: The transmission measurement setup uses separate transmit (Tx) and receive (Rx) paths to capture signal propagation through the hand to the contacted surface.

(c) S_{11}: The reflection measurement setup uses the same path for Tx and Rx to analyze impedance transitions at the injection site and the hand-material interface.

Fig. 2. Equivalent Circuit and Measurement Configurations for Electrical Impedance Sensing.

3.3 Impedance Measurement Techniques

This paper explores impedance sensing with wideband frequency sweeps, a technique offering rich insights into hand characteristics and enabling diverse interactions, as demonstrated in [47]. Traditional bioimpedance measurement approaches include single- or multi-frequency impedance analysis, typically operating within the frequency range of 5 kHz to 1 MHz [43]. For applications demanding higher frequency measurements, several hardware options exist, each with distinct trade-offs.

High-end bioimpedance analyzers, such as [46], offer extended bandwidth capabilities for measurements at higher frequencies but come at a premium cost. Custom-built systems provide affordability but require specialized design expertise and validation. Software-defined radios (SDRs), while versatile, are limited by their narrow instantaneous bandwidth, necessitating multiple sweeps for wideband measurements [12].

Vector network analyzers (VNAs) emerge as a compelling alternative, offering precise, wideband measurements across a broad frequency spectrum in a single sweep, ideal for characterizing complex impedance variations

[33]. Recent advances, notably the advent of hobbyist-grade, low-cost VNAs like the NanoVNA [6], have further democratized access to this powerful measurement tool, opening new avenues for impedance sensing research and applications [22, 23, 47].

Two standard methods exist for measuring impedance with a vector network analyzer (VNA) when the device under test (DUT) is the hand: an S_{11} measurement (one-port reflection) or an S_{21} measurement (two-port transmission).

The S_{11} method (Figure 2c) measures the reflection coefficient, which quantifies the fraction of the incident signal that is reflected back from the DUT. In this configuration, a single electrode is placed on the wrist, with the VNA port serving as both the signal source and receiver. The complex impedance (Z) of the DUT can be derived from the measured S_{11} parameter using:

$$Z = Z_0 \frac{1 + S_{11}}{1 - S_{11}}, \tag{5}$$

where Z_0 is the characteristic impedance of the measurement system, typically 50 Ω. The magnitude of S_{11} indicates the degree of impedance mismatch: larger $|S_{11}|$ values correspond to greater mismatch between the DUT impedance and Z_0, while $S_{11} = 0$ indicates perfect matching ($Z = Z_0$).

The S_{21} method (Figure 2b) measures the transmission coefficient, which quantifies the fraction of the signal transmitted from port 1 to port 2 through the DUT. In this configuration, one electrode is placed at the proximal position (e.g., near the wrist or ulnar styloid process, a common watch-wearing location), connected to port 1, while a second electrode is placed at a distal position (e.g., on the hand or finger), connected to port 2. The impedance can be estimated from the measured S_{21} parameter. For a series impedance model where the DUT is inserted between matched ports, the relationship is:

$$Z = Z_0 \frac{2(1 - S_{21})}{S_{21}}, \tag{6}$$

Lower $|S_{21}|$ values indicate greater signal attenuation through the DUT, corresponding to higher impedance or increased path loss.By analyzing frequency-dependent S_{11} and S_{21} parameters, we can extract comprehensive impedance profiles of the hand, enabling precise characterization for touch and interaction sensing applications.

3.4 Impedance Sensing Challenges and Solutions for Robust On-world Touch Detection

To enable Z-Band to successfully and robustly detect touch on external surfaces, aka on-world touches from the wrist, three key requirements must be met.

First, there must be a *non-line-of-sight (NLoS) signal transmission* through the hand and fingers that is modulated by the contacted surfaces. Since the Z-Band operates from the wrist, the RF signals must effectively propagate through the hand and interact with external materials. This ensures that the resulting impedance changes can still be detected even when the fingers make contact with a surface that is not directly visible to the sensing system.

Second, the *return signal change must be large and sufficiently unique* to yield a distinguishable difference between different touch conditions. A small, ambiguous change in impedance would make it difficult to differentiate between different contact events and surface types.

Third, Z-Band must be *highly sensitive* to detect touches even when the contacted material is *ungrounded* (i.e., not connected to a reference ground) or is *strongly dielectric* (i.e., has very low electrical conductivity). Detecting touch interactions in such cases is particularly challenging for impedance-based sensing systems. Typically, impedance sensing relies on measurable changes in electrical properties when contact occurs. However, ungrounded materials or highly dielectric surfaces do not easily alter the electrical impedance, making them harder to detect.

To overcome these challenges, Z-Band leverages:

- **High-frequency signal propagation** to ensure that even in non-line-of-sight conditions, signals travel effectively through the hand and fingers to interact with external materials.
- **Broadband impedance sensing** to capture subtle variations in impedance across a range of frequencies to improve detection robustness.
- **Higher transmit signal strength** to ensure reliable sensing. We designed a *custom RF front-end* for the vector network analyzer (VNA), enabling increased transmission power and improved signal-to-noise ratio (SNR). This enhancement compensates for signal attenuation through biological tissues and enables clearer detection of impedance changes across different materials.

By meeting these criteria, Z-Band ensures reliable on-world touch sensing in diverse real-world conditions, even on materials that are traditionally difficult for impedance-based detection systems.

4 BACKGROUND EXPERIMENTS

After conducting a theoretical analysis, we perform simulations to evaluate how key parameters influence impedance sensing. Specifically, we examine *transmit frequency, electrode geometry,* and *contact with different materials*.

4.1 Key Parameters Influencing Impedance Sensing

4.1.1 Frequency. Frequency significantly impacts impedance-based sensing, affecting signal penetration and sensitivity to surface interactions. The layered structure of the human hand, with varying electrical properties in each layer (skin, fat, muscle, blood), creates a complex electrical environment. Biological tissues exhibit a frequency-dependent impedance response due to the electrical characteristics of cells, membranes, and fluids [2, 34]. Different frequency bands offer distinct advantages and disadvantages for touch sensing. Table 2 summarizes the effects of different frequency bands on impedance sensing.

Table 2. Frequency-dependent characteristics of bioimpedance measurements and their implications for touch sensing [2, 34]. At low frequencies, high membrane impedance confines current to extracellular pathways with deep penetration. At high frequencies, reduced membrane impedance allows transmembrane current flow, but increased electrode-skin impedance mismatch and skin effect limit penetration depth, enhancing surface sensitivity.

Frequency Band	Dominant Current Pathway and Tissue Response	Penetration Depth	Surface Sensitivity
kHz (typically <100 kHz)	Extracellular pathways (high membrane reactance blocks intracellular current)	Deep	Low
100 kHz – Few MHz	Transition region (progressive membrane penetration; mixed intra- and extracellular current)	Moderate	Moderate
Tens of MHz and above	Both pathways are accessible (low membrane reactance), but surface-confined due to skin effect and electrode impedance mismatch	Shallow	High

This interplay between frequency, tissue characteristics, and measurement objectives necessitates careful selection of operating parameters to optimize the depth and sensitivity of impedance measurements for the given application.

4.1.2 Electrode Geometry. Electrode geometry is crucial in impedance-based touch sensing, impacting signal injection, detection, and overall measurement accuracy. *Size of electrodes* affects the electric field distribution and sensitivity to impedance changes. Larger electrodes offer better skin contact and stronger signal transmission due to lower contact impedance but may be less sensitive to overall impedance changes; smaller electrodes, despite higher contact impedance, can be more sensitive to changes in impedance. *Electrode shape* influences the electric field distribution and current density at the electrode-skin interface, with sharp corners concentrating the field and potentially affecting accuracy, while smoother contours offer a more uniform current distribution. In our simulations, we favored round electrodes due to their ability to generate a uniform electric field when injected at the center, ensuring consistent signal distribution across the measurement area [33].

The influence of electrode geometry also depends on *frequency*. At lower frequencies, the electric field is less focused, making electrode geometry less critical. However, at higher frequencies, the field becomes concentrated, increasing the impact of electrode geometry and potentially leading to edge effects and non-uniformities that can affect accuracy. This necessitates careful consideration of electrode size at different frequencies. While *material* also plays a role, our simulations and prototyping focused on gold electrodes, a common choice for bioimpedance applications.

4.1.3 External Contact. External contact alters the hand's overall impedance. When the hand touches a surface, the signal through the hand encounters a new interface with different conductivity and permittivity, affecting the measured impedance. Contacting a conductive material provides a low-resistance path, leading to a decrease in impedance as the current is diverted through the conductive surface. Conversely, contacting an insulator hinders the current flow, potentially increasing impedance as the current seeks alternative paths within the hand. Analyzing these impedance changes during external contact provides valuable information about the contact state and the contacted material's electrical properties.

4.2 Simulation

We used finite integration technique (FIT) simulations with CST Studio Suite, which offers 3D electromagnetic (EM) analysis capability. We selected a frequency range from 1 MHz to 1 GHz, guided by research demonstrating substantial attenuation of wave propagation through the body beyond 1 GHz [34, 47]. We then constructed a detailed bio-model of a 38-year-old male (180 cm, 103 kg) using the CST Bio Models Library[1] and data from the US National Library of Medicine's Visible Human Project.[2] The model included 31 distinct tissue types, such as blood, bone, fat, muscle, and skin, with a resolution of $1 \times 1 \times 1$mm. To optimize computational efficiency, the simulation focused on the right forearm and hand, isolating them from the rest of the body.

4.2.1 Signal Propagation Analysis. Understanding how RF signals propagate through the hand is critical for determining the optimal frequency range for Z-Band. The human hand is a complex, lossy medium composed of multiple layers, including skin, fat, muscle, and bone, each exhibiting distinct electrical properties. These layers differ in conductivity, permittivity, and water content, all of which vary with frequency, influencing signal attenuation and propagation efficiency.

For Z-Band to function reliably, we needed to identify a frequency range that enables efficient signal transmission from the wrist to the fingers. Since signal strength diminishes as it propagates through the body, selecting an appropriate frequency ensures that sufficient signal reaches the interaction site, enabling robust sensing.

[1] https://space.mit.edu
[2] https://www.nlm.nih.gov

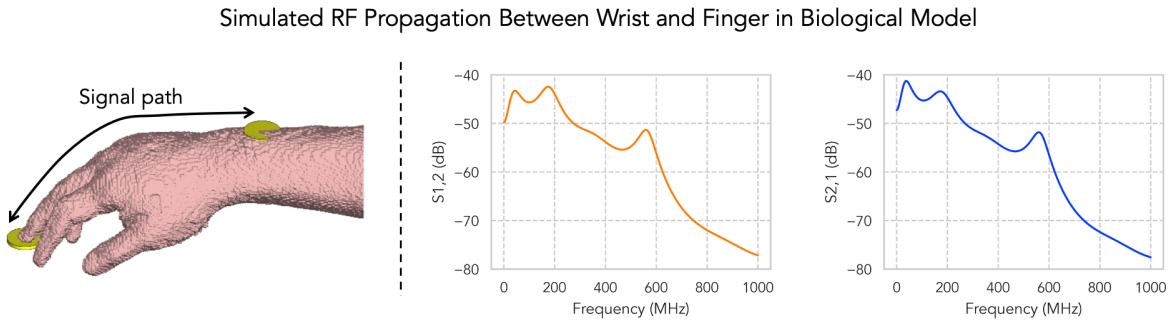


Fig. 3. Simulated RF propagation between the wrist and finger using a biological hand model in CST Studio Suite. The left panel shows the simulated signal path between electrodes placed at the wrist and fingertip. The right panels display the simulated S_{12} and S_{21} results, illustrating RF attenuation and propagation characteristics through the hand model.

Experiment Setup. To investigate frequency-dependent propagation, we conducted an experiment in which an RF signal was injected at the wrist and measured at the tip of the middle finger. The middle finger was chosen because it represents the longest path from the wrist, providing insight into signal attenuation over the maximum propagation distance. We show our experiment setup in Figure 3. We performed a broadband frequency sweep from 1 kHz to 1000 MHz to evaluate signal transmission across a wide frequency range.

Results and Observations. The results of our experiments, shown in Figure 3, indicate that higher frequencies propagate more effectively on the skin from the wrist to the fingertip than lower ones. As discussed in Section 3.1, this observation is primarily due to the way different frequencies interact with the layered composition of the hand. Higher-frequency signals tend to be confined along the skin's surface rather than penetrating deeper tissues; lower-frequency signals penetrate deeper into the hand due to their longer wavelengths. This phenomenon results in more substantial signal loss before reaching the fingers, making them less effective for touch detection. These findings highlight the advantage of selecting higher frequencies for Z-Band since they better balance propagation efficiency and sensitivity to surface interactions.

To validate our simulation findings, we repeated the propagation experiments with real users (N=5) and recorded S-parameter measurements using electrode placement as in the CST simulation. Figure 4 presents the measured S_{21} results from these real-world evaluations. Broadly, we observe similar trends between the simulated and real measurements: S_{21} values are higher at lower frequencies and gradually decrease as the frequency increases. In the real measurements, we also note a distinct drop at around 300 MHz, likely due to resonance effects or impedance mismatch, factors that are harder to control in physical experiments. The overall signal strength observed in the real-world measurements is stronger than in simulation, perhaps attributable to the presence of skin moisture and sweat in actual use, which increases skin conductivity and can facilitate RF wave propagation. While the overall trend aligns well, the simulated and real-world curves are not expected to match exactly due to differences in biological variability, tissue composition, sensor alignment, and hardware-induced artifacts. Nevertheless, the close correspondence between simulated and empirical data supports the reliability of our modeling approach.

4.2.2 Electrode Size and Its Impact on Impedance Sensing. To understand how electrode size influences impedance sensing, we tested round electrodes of varying radii (1.25 mm, 2.5 mm, 5 mm, 10 mm, and 15 mm) while sweeping through a broad frequency range from 1 kHz to 1000 MHz. In this experiment, a single electrode was placed on

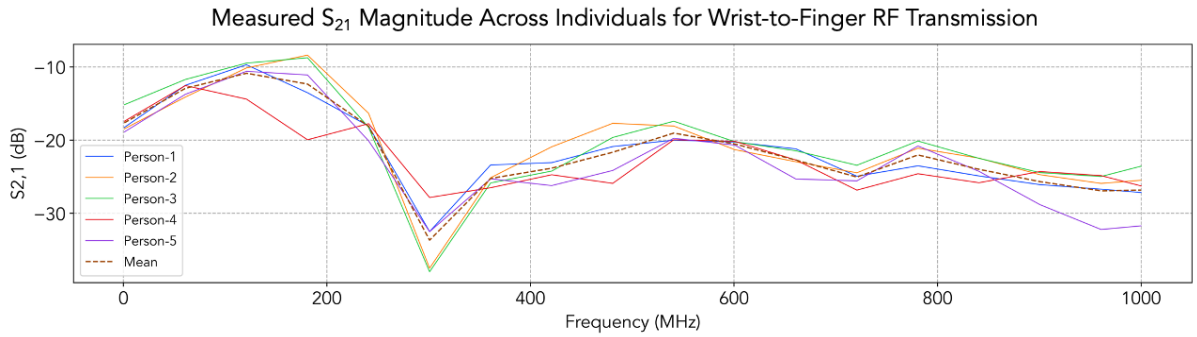


Fig. 4. Measured S_{21} magnitude (in dB) across frequency from 1 MHz to 1000 MHz for five individuals, showing variation in RF wave propagation from wrist to finger.

top of the wrist for S_{11} measurements, while an additional electrode was positioned at the bottom of the wrist to capture S_{21} signals.

Figure 5 demonstrates how electrode radius impacts RF sensing performance in smartwatch applications from 0-1000 MHz. Larger electrodes (15 mm) achieve optimal impedance matching ($S_{11} \approx -0.4$ dB at 1 GHz) and signal transmission ($S_{21} \approx -20$ dB at low frequencies), while smaller electrodes show significant degradation (1.25 mm: $S_{21} \approx -65$ dB at 1 GHz). Better performance of larger electrodes is attributable to their lower contact impedance, which enhances signal transmission efficiency [26, 34]. For smartwatch design, this creates a trade-off between performance and form factor. *Large electrodes (10-15 mm)* are ideal for flagship devices with spacious case backs, providing robust sensing across the full frequency spectrum and resilience to contact variations—optimal precise bioimpedance analysis. *Medium electrodes (5 mm)* suit compact or fashion-oriented designs where case back space is constrained, offering acceptable performance (10-15 dB reduction) especially below 500 MHz. *Small electrodes (1.25-2.5 mm)* present significant challenges for smartwatch applications due to substantial signal attenuation, which requires additional amplification circuitry and may result in reduced signal-to-noise ratio. While feasible with appropriate signal processing techniques, they are best suited for applications where extreme miniaturization outweighs the need for optimal signal quality. The choice depends on application requirements: precise sensing demanding high signal fidelity benefits from larger electrodes, while basic sensing tasks can effectively utilize medium-sized alternatives.

We repeated this experiment with three users using gold-coated copper electrodes fabricated on a flexible PCB and cut into circular shapes of varying diameters. We collected the similar S-parameter measurements and observed similar trends: electrodes with larger diameters consistently provided better performance, likely due to improved skin contact area and reduced impedance mismatch.

4.2.3 Impact of Touching External Surfaces on Impedance Sensing. To assess how different external surfaces influence impedance sensing, we examined interactions with commonly encountered materials: metal (copper), plastic (epoxy resin), and wood. In our CST simulations, these surfaces were modeled uniformly with dimensions of $100 \times 100 \times 3$mm, varying only in material-specific properties such as conductivity and loss tangent. The simulation setup, depicted in Figure 6, was designed to analyze how these materials affect S_{11} and S_{21} signal responses when touched, with the sensing electrodes being positioned at the wrist.

Simulation results revealed distinct variations in S_{11} and S_{21} signals depending on the material of the contacted surface. While these variations may appear subtle, previous research [47, 60] has demonstrated that even small deviations—on the order of 0.1 dB in S_{11}—can be effectively utilized for surface classification. By employing a broad

frequency sweep rather than single-point measurements, our approach captures a comprehensive impedance profile, enabling machine learning models to leverage variations across the frequency spectrum.

We present real-world data showing how the signal changes when touching different external surfaces in Section 5, where we designed and tested multiple AFE (Analog Front-End) systems to capture impedance signals. The trends observed in that section closely align with the simulation results presented here, reinforcing the consistency and reliability of the modeled behavior.

In summary, the simulations validated the feasibility of wrist-based impedance sensing for accurately detecting touch interactions.

5 IMPEDANCE SENSING FRONT-END ARCHITECTURES FOR VNA

5.1 Challenges and Solutions for Wrist-Based Impedance Sensing with VNAs

VNAs have been successfully used for impedance-based interaction detection, including applications that inject signals into the body or use air coupling [22, 24, 47]. However, a key challenge arises when injecting the signal at the wrist to detect interactions at the fingers.

Research Question: Can a portable VNA accurately measure impedance for hand interactions when signal injection occurs at the wrist given the constraints of signal attenuation and low transmission power?

The human body acts as a *lossy transmission medium*, significantly attenuating signals as they travel through tissue. This attenuation, combined with the inherently low transmission power of portable VNAs such as the NanoVNA, make direct signal injection impractical without amplification. However, amplification introduces another challenge: Simply adding an amplifier at the VNA's S_{11} (TX) port is not possible because amplifiers isolate reverse signals, allowing the amplified forward signal to pass but blocking the reflected signal needed for accurate S_{11} measurement. On the other hand, the S_{21} measurement, which uses a separate RX port, allows amplification. However, amplification in S_{21} can still introduce signal distortion and must be carefully designed to ensure accurate impedance calculations.

Proposed Solution: External Analog Front Ends (AFEs). To overcome these challenges, we introduce external *analog front ends* (AFEs) designed to interface with the VNA. We developed three distinct prototype designs to address signal amplification for hand interaction detection. Two designs explore amplified S_{11} measurements,

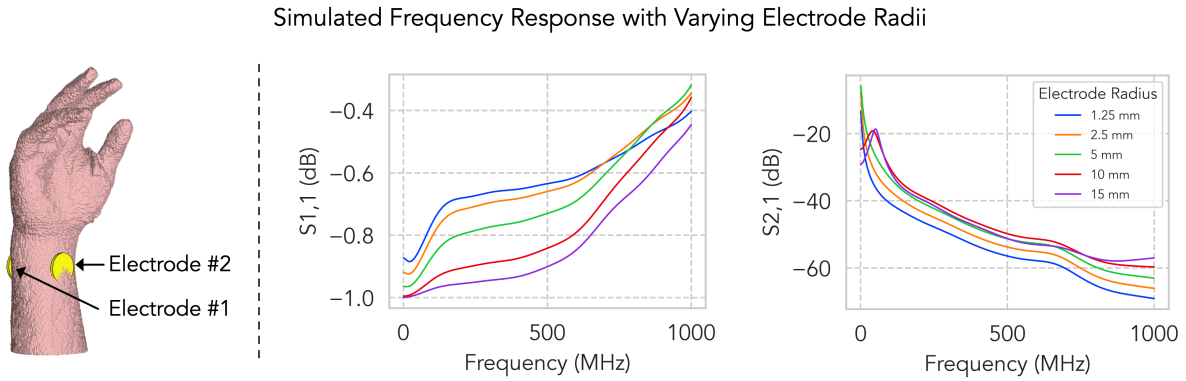


Fig. 5. CST Studio Suite simulation showing the effect of electrode radius on RF performance. (Left) Hand model with electrode placement on the wrist. (Center, Right) Simulated S_{11} and S_{21} results for varying electrode radii, indicating that the 15 mm electrode radius achieves the best overall signal quality.

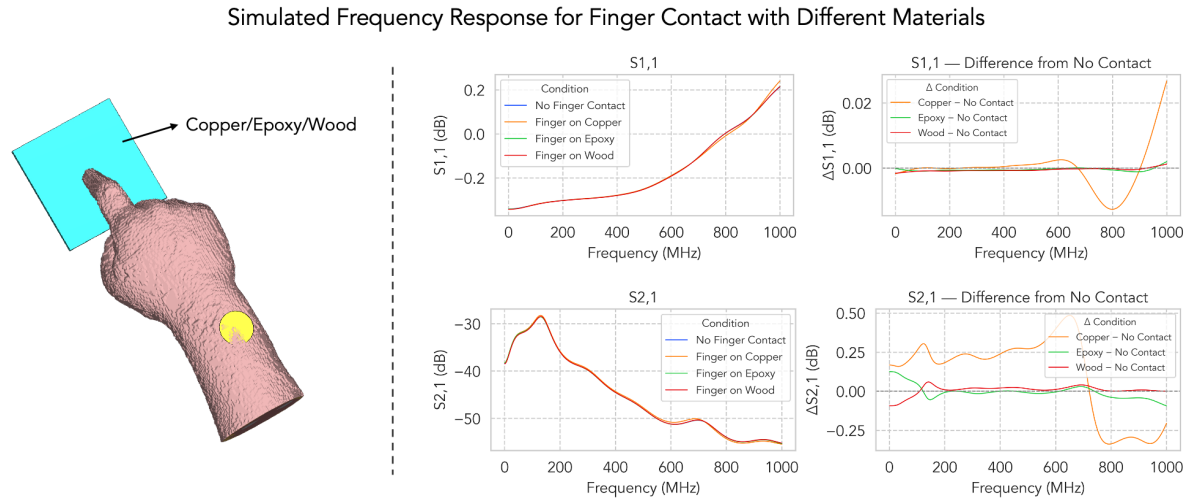


Fig. 6. CST Studio Suite simulation showing RF response for finger contact with different surface materials. (Left) Simulation setup with electrode placement and hand contacting copper, epoxy, and wood surfaces. (Center) Simulated S_{11} and S_{21} results and their differences (Right) from the no-contact condition, illustrating that wrist-based impedance sensing distinguishes material-dependent signal variations.

while the third focuses on amplified S_{21} measurements. While these architectures theoretically measure the same impedance changes, their practical implementations introduce variations due to component characteristics, signal attenuation, noise from longer paths, and differences in coupling with the body.

Experimental Evaluation of Designs. To assess these designs, we implemented each architecture and conducted controlled experiments under comparable conditions. The impedance response was analyzed across different surfaces, aligning with the experiment setup in Section 4. This comparative study provided insights into each design's practical trade-offs and guided the selection of the optimal architecture for Z-Band.

Implementation Details. For all implementations, we used the LiteVNA [11], an enhanced version of the NanoVNA with improved performance. Though its default sweep rate is approximately 5 Hz, we leveraged an experimental firmware feature to increase the sampling rate to 30 Hz.[3] For signal amplification, we selected the Mini-Circuits LHA-13LN+ amplifier, which offers a 22 dB gain, a 1-1000 MHz bandwidth, and a low noise figure of 1.1 dB, ensuring minimal signal degradation. We used round, flexible, gold-coated copper electrodes with a 15 mm radius; the choice of gold coating ensures high conductivity, oxidation resistance and biocompatibility, while the flexible design improves comfort and adaptability to wrist contours. For S_{11} measurements, a single electrode was placed on the top of the wrist, near the ulna area. For S_{21} measurements, two identical electrodes were positioned—one atop the wrist (near the ulna, connected to the S_{11} port) and another on the bottom of the wrist (connected to the S_{21} port). All prototypes were battery-powered, with a Raspberry Pi handling VNA data collection and Wi-Fi streaming, allowing a fully wireless system.

[3]The sweep time of LiteVNA can be decreased by writing the value 0x01 to registers at addresses 0xE0 and 0xE1.

5.2 Design 1: Dual-circulator Reflectometry

In the first design, we used *circulators* to perform S_{11} measurements. Figure 7b shows the prototype for this design. This RF architecture, shown in Figure 7a, employs two circulators to amplify the transmitted signal, measure the reflected signal, and isolate between stages. RF circulators are passive, non-reciprocal three-port devices that control the direction of signal flow in a circuit. A signal entering port 1 will exit port 2, one entering port 2 will exit port 3, and one entering port 3 will exit port 1.

The outgoing RF signal from the VNA enters port 1 of circulator 1, which directs it to port 2, connected to a power amplifier (PA). The amplified signal then passes through circulator 2 from port 1 to port 2 and is coupled to the body via body electrodes. The reflected RF signal from the body enters port 2 of circulator 2, which directs it to port 3. This signal then uses an RF attenuator to reduce its power before entering port 3 of circulator 1, safeguarding the VNA from damage. Circulator 1 directs the attenuated reflected signal to port 1, which is connected to the VNA for measurement and analysis.

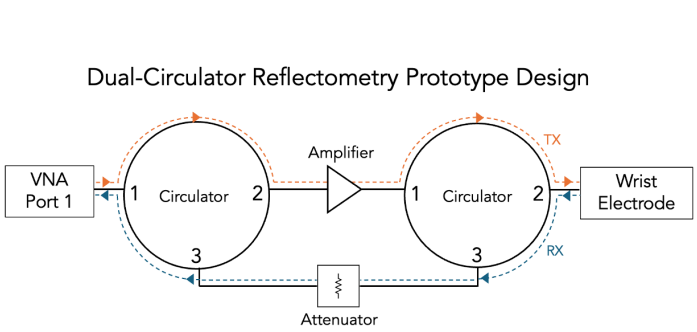
In this architecture, circulator 2 isolates the PA from the reflected signal by directing any energy entering port 2 to port 3, preventing potential damage. Similarly, circulator 1 isolates the VNA from the PA, protecting it from the high-power amplified signal. Both circulators collectively isolate the VNA from the high-power PA and the reflected signal, preventing interference and potential damage. *This architecture enables higher TX power, bidirectional signal flow, measurement of the reflected signal, and isolation of each stage, leading to accurate and reliable measurements.*

Though wideband sweeps were desired, practical limitations of sub-GHz circulators, typically exhibiting bandwidths less than 100 MHz, necessitated a narrower sub-GHz bandwidth for our implementation. Our frequency selection is driven by simulation, component constraints, and empirical testing. CST simulations revealed peak sensitivity to hand pose changes in the 1-500 MHz range, with other frequencies also showing signal variations. By balancing the need for high sensitivity and propagation (favored at higher frequencies) with deeper biotissue penetration (characteristic of lower frequencies) [34], while also considering the practical limitations of available circulator bandwidths, we ultimately selected the 100-150 MHz range as our operational bandwidth. We therefore chose the TH6060ES circulator, manufactured by RFTYT Technology, for our implementation. Figure 7c shows the S_{11} curves for different scenarios using this prototype.

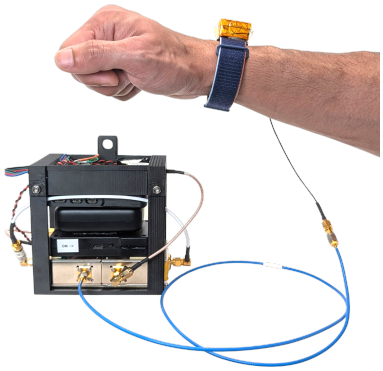
5.3 Design 2: Coupler Reflectometry

In design prototype 1, circulators redirect the reflected signal back to the S_{11} port, enabling the use of the S_{11} port for both transmission and reception. However, in design prototype 2, we use an *RF coupler* to redirect the reflected signal to the S_{21} port for measurement. A *coupler* is a passive RF device with four ports that samples a portion of the signal in the forward direction and any reflected signal in the reverse direction, enabling simultaneous monitoring without disrupting the main signal path. *This approach requires only a single coupler instead of two circulators and benefits from the wider bandwidth typically available with couplers, even at lower frequencies.* Specifically, we employ the MiniCircuits SCBD-16-63HP+ coupler with a bandwidth of 50 MHz to 1000 MHz for this prototype (see Figure 8b.)

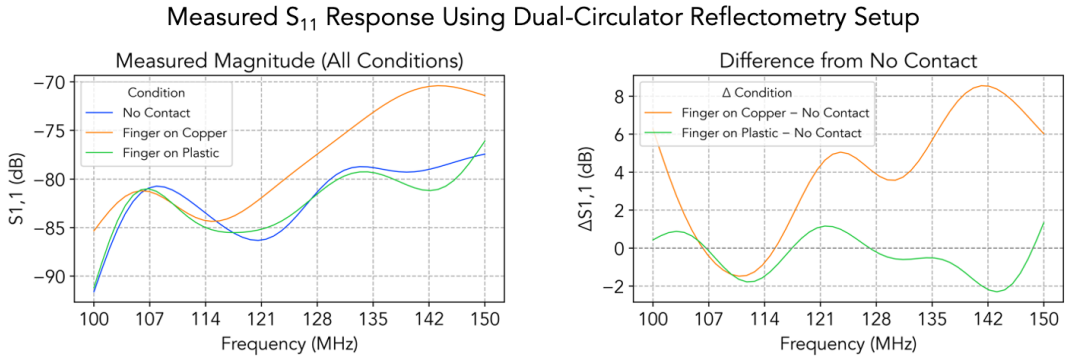
When a coupler is connected to the S_{11} port and the reflected signal is routed to the S_{21} port, the captured S_{21} signal becomes a combination of reflections from both the DUT (a hand, in this case) and the coupler itself, along with any signal leakage. This contrasts with direct S_{11} measurement, where the captured signal purely represents the DUT's reflection. However, assuming that the coupler's characteristics and signal leakage remain constant for a given frequency, changes in the acquired S_{21} signal primarily signify variations in the DUT's reflection, letting us indirectly infer changes in the DUT's impedance. Figure 8a illustrates the architecture for this prototype and 8c shows the S_{11} curves for different scenarios with this prototype.



(a) System design illustrating the transmit (Tx) and receive (Rx) signal paths using two circulators, an amplifier, and attenuator for impedance-based sensing at the wrist.



(b) Prototype implementation of the circulator-based measurement setup.



(c) Measured S_{11} responses showing reflection magnitude (left) and difference from the no-contact condition (right), demonstrating sensitivity to material contact (copper vs. plastic).

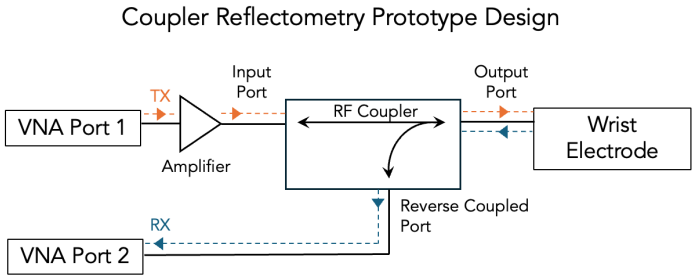
Fig. 7. Design 1: Dual-circulator reflectometry prototype and measured response.

5.4 Design 3: Through Transmission Design

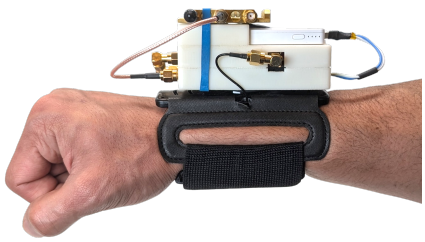
The previous two approaches used S_{11} for sensing. In contrast, this method employs S_{21} for measurement, *requiring minimal external hardware since two ports are inherently available for this purpose.* Figure 9b shows the prototype design. We connect an amplifier to the S_{11} port's output, which is then linked to an electrode on top of the wrist. Another electrode, placed at the bottom of the wrist, connects to the S_{21} port. Figure 9a shows this design, and 9 shows the S_{21} curves for different scenarios for this prototype.

5.5 Comparison of Designs and Trade-offs

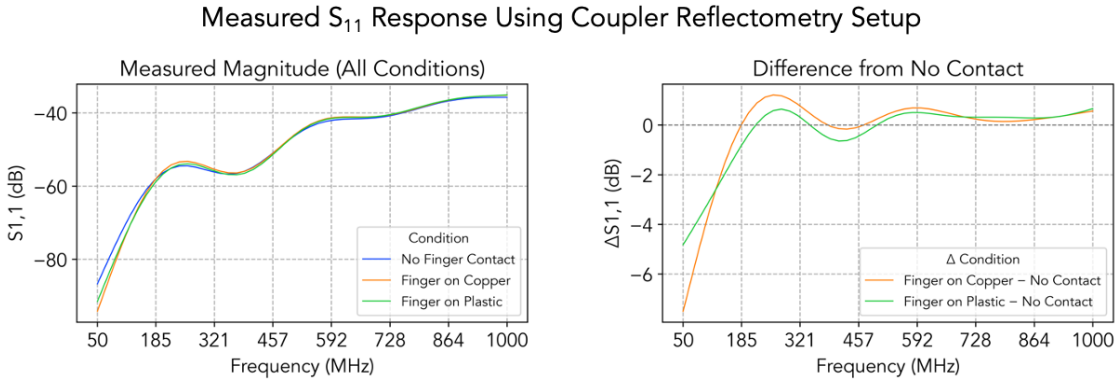
All three architectures exhibited clear changes in response to different hand poses and contact with various surfaces, reproducing the patterns observed in the simulations. However, each design presented distinct performance characteristics and tradeoffs. Table 3 summarizes these tradeoffs.



(a) System design showing transmit (Tx) and receive (Rx) signal paths through an RF coupler, amplifier, and wrist electrode for impedance sensing.



(b) Prototype implementation of the coupler-based measurement setup.

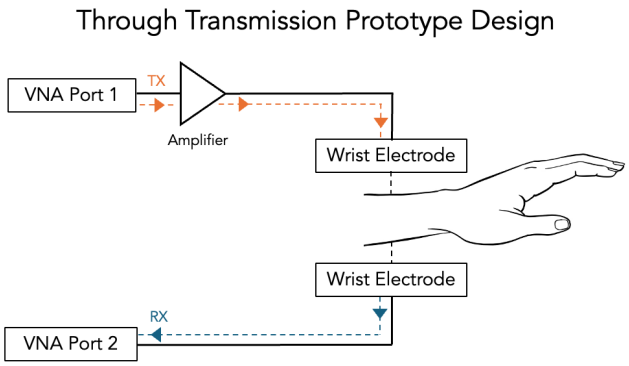


(c) Measured S_{11} responses showing reflection magnitude (left) and difference from the no-contact condition (right), demonstrating that the coupler reflectometry design detects material-dependent impedance changes at the wrist.

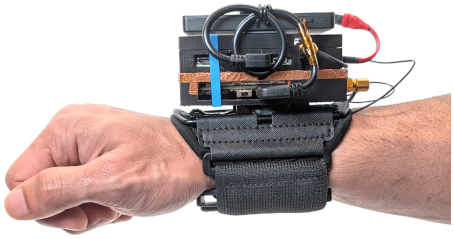
Fig. 8. Design 2: Coupler-based reflectometry prototype and measured response.

Design 1 (dual-circulator) The dual-circulator reflectometry design (Figure 7) demonstrates effective material detection capabilities in the 100-150 MHz range. The measured S_{11} responses show clear differentiation between no-contact, finger-on-copper, and finger-on-plastic conditions, with copper contact producing up to 8 dB difference from the no-contact baseline around 135 MHz. The system successfully isolates transmit and receive paths using circulators, enabling sensitive reflection measurements at a single wrist electrode location. However, this design requires two RF circulators, an amplifier, and an attenuator, resulting in a complex and space-intensive implementation unsuitable for compact wearables. The operational frequency range is limited to 100-150 MHz, restricting the ability to perform wideband impedance analysis. Additionally, circulators are costly components that increase both system complexity and power consumption, making this approach less practical for consumer smartwatch applications despite its good sensing performance.

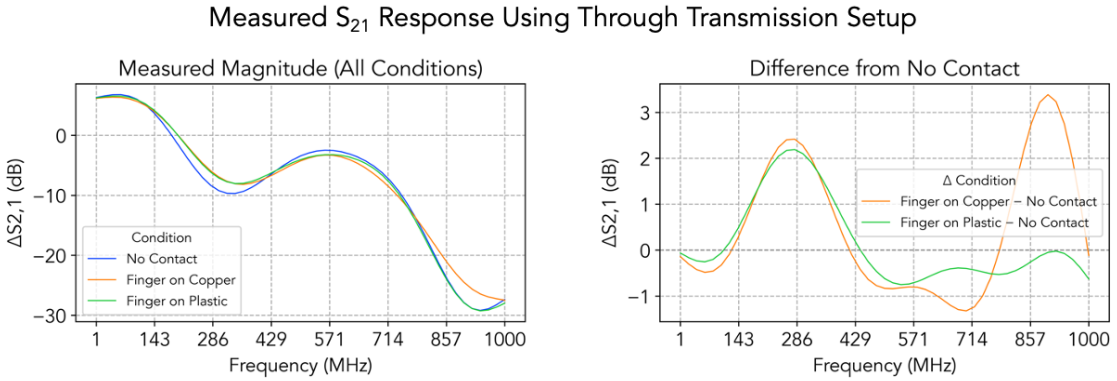
Design 2 (coupler) The coupler-based reflectometry design (Figure 8) achieves material-dependent impedance detection across a broader frequency range (50-1000 MHz) compared to the circulator design. The measured S_{11} responses demonstrate sensitivity to contact materials, with copper and plastic contacts producing distinguishable impedance changes relative to the no-contact condition. Peak differentiation occurs around 185 MHz, with approximately 1-2 dB difference between materials. The design simplifies the signal path by replacing circulators



(a) System design showing transmit (Tx) and receive (Rx) signal paths through separate wrist electrodes and an amplifier for impedance-based transmission sensing.



(b) Prototype implementation of the through-transmission measurement setup



(c) Measured S_{21} responses showing transmission magnitude (left) and difference from the no-contact condition (right), demonstrating the ability of the through-transmission design to capture material-dependent signal variations across the wrist

Fig. 9. Design 3: Through-transmission prototype and measured response.

with a single RF coupler, reducing component count and system complexity. While more compact than the circulator approach, the coupler design exhibits lower sensitivity to material changes, with difference magnitudes of only 1-2 dB compared to the 8 dB achieved by the circulator system. The coupler introduces insertion loss in both transmit and receive paths, reducing overall signal-to-noise ratio. Additionally, the reverse coupled port provides inherently weaker signal coupling compared to circulator isolation, requiring careful amplifier design to achieve adequate sensitivity. The design still requires both an amplifier and RF coupler, limiting further miniaturization for ultra-compact wearables.

Design 3 (through-transmission) The through-transmission design (Figure 9) provides the simplest hardware implementation, requiring only an amplifier and two wrist electrodes without any circulators or couplers. The measured S_{21} responses demonstrate robust material detection across an ultra-wideband frequency range (1-1000 MHz), with clear differentiation between copper and plastic contacts. This design offers the widest

frequency coverage of the three approaches, enabling comprehensive impedance spectroscopy for diverse sensing applications. The primary limitation is the requirement for two spatially separated electrodes on the wrist, which may constrain placement flexibility and increase the required device footprint compared to single-electrode designs. The spatial separation also means the measured impedance represents a specific tissue path between electrodes rather than a localized measurement at a single point. Additionally, while the hardware is simplified, the through-transmission measurement is more susceptible to electrode contact quality variations at both sites, as poor contact at either electrode degrades the overall signal. Despite these limitations, the dramatic reduction in RF component complexity, cost, and size makes this design the most practical for integration into compact smartwatch form factors.

As shown in Table 3, the three designs present distinct trade-offs: the dual-circulator approach achieves the highest sensitivity (8 dB) but suffers from the largest form factor and highest complexity; the coupler design offers moderate performance across all metrics; and the through-transmission design provides the widest bandwidth and simplest implementation at the cost of requiring two electrodes and moderate sensitivity.

Ultimately, the choice of design depends on the specific application's requirements and priorities. Design 1, with its high isolation and potential for high sensitivity, might be ideal for applications demanding precise impedance measurements, such as medical diagnostics or detecting subtle changes in grip force. Design 3, with its simplicity and minimal components, is well-suited for compact and cost-sensitive devices where high sensitivity is not critical.

We selected Design 3 for implementation based on its optimal trade-off between sensing performance and practical wearable constraints. The through-transmission approach sacrifices some sensitivity relative to the circulator design but delivers three critical advantages: (1) ultra-wideband frequency coverage (1-1000 MHz) enabling diverse sensing modalities, (2) minimal hardware requiring only an amplifier rather than bulky RF components, and (3) straightforward integration into smartwatch form factors. The 2-3 dB sensitivity proves sufficient for reliable material detection. This makes Design 3 the most viable solution for our prototype.

Table 3. Comparison of three reflectometry designs for wrist-worn impedance sensing.

Characteristic	Dual-Circulator	Coupler	Through-Transmission
Frequency Range	Narrowest (50 MHz)	Wide (950 MHz)	Widest (999 MHz)
Sensitivity (Peak Δ)	Highest (8 dB)	Lowest (1–2 dB)	Moderate (2–3 dB)
Hardware Complexity	Highest (2 circulators)	Moderate (1 coupler)	Lowest (amplifier only)
RF Component Count	4 (circulators, amplifier, attenuator)	2 (coupler, amplifier)	1 (amplifier)
Electrode Count	Fewest (1)	Fewest (1)	Most (2)
Physical Form Factor	Largest	Medium	Smallest
Estimated Cost	Highest	Medium	Lowest
Wearable Suitability	Least suitable	Moderately suitable	Most suitable

6 Z-BAND PROTOTYPE

Based on the simulation and experiment results from Sections 5 and 4, we built the Z-Band prototype using the through transmission RF design (design 3).

Though impedance sensing performed well in our experiments, we found that real-world scenarios introduced additional factors impacting signal quality. Variations in body anatomy, external RF interference, and motion artifacts due to electrode movement can all introduce noise. Although RF-based systems are indeed sensitive to motion-induced artifacts—particularly due to variations in electrode-skin contact—this sensitivity is generally lower than that of inertial systems. IMUs often register all motion equally, making it difficult to distinguish between incidental limb movement and intentional interaction. In contrast, RF impedance sensing responds primarily to contact-driven changes in body conductivity, enabling better discrimination between touch events and background motion.

While RF provides the primary sensing signal, IMU data can complement it by capturing motion context—allowing the system to filter out noise in high-motion scenarios or disambiguate gestures that involve movement. By combining both modalities, our system gained spatial awareness that helped distinguish intentional interactions from environmental noise and even supports novel touch-plus-motion interactions. Thus, our final Z-Band system consists of both through-transmission impedance sensing and an IMU, leveraging their complementary strengths for robust and versatile interaction capabilities.

Our Z-Band implementation prototype (Figure 11a), used for user evaluation and testing, mirrored the design outlined in Section 5.4, incorporating the same components: LiteVNA, amplifier, and Raspberry Pi Zero 2W. Figure 10 shows an overview of the system, and Figure 11b shows an internal view of the prototype. The components were housed in a 3D-printed enclosure that was secured to the user's hand with a Velcro wristband. The frequency sweep was configured from 300MHz to 800MHz, aligning with the findings from Section 5. Within the 300-800 MHz band, the system achieves consistent 2-3 dB material differentiation with sufficient signal strength for robust detection across varying user conditions. The IMU used was ISM330DHCX, which was connected to an nRF52840 microcontroller and relayed data to the Raspberry Pi via UART. The flexible electrodes (radius=15mm) were mounted on a 1 cm thick foam to ensure conformability to the user's hand while maintaining uniform pressure. Figure 11c shows the electrodes used. The sensor data was grouped into batches to minimize latency and transmitted via TCP sockets over Wi-Fi to a laptop, where it was processed using a Python-based analysis program. The prototype weighed about 285 gms and consumed 0.7 Amp of current at 5V.

While Z-Band is designed as a wearable system, our current prototype is larger and heavier than conventional wearable devices. This increased size stems from using general-purpose components such as a full vector network analyzer (VNA), development boards, and a Raspberry Pi, which were selected to support rapid iteration and flexible prototyping. These components also require a higher-capacity battery, further adding to the overall bulk. While this configuration is not intended for daily use, it let us quickly validate the feasibility and robustness of our sensing approach across diverse scenarios with real users. To demonstrate the potential for wearable deployment, we developed a more compact version of Z-Band (see Figure 1) using custom analog front-end circuitry, discussed further in Section 9.

We see a clear path to miniaturizing Z-Band into a practical, wrist-wearable form factor comparable to a smartwatch. Section 10.3 outlines strategies for replacing general-purpose hardware with low-power embedded processors and custom RF modules or ASICs. These changes would not only reduce size and weight but also significantly lower power consumption, enabling always-on operation suitable for everyday use. We anticipate that with miniaturized hardware and material optimization, Z-Band can be made comfortable and energy-efficient enough for continuous, long-term wear.

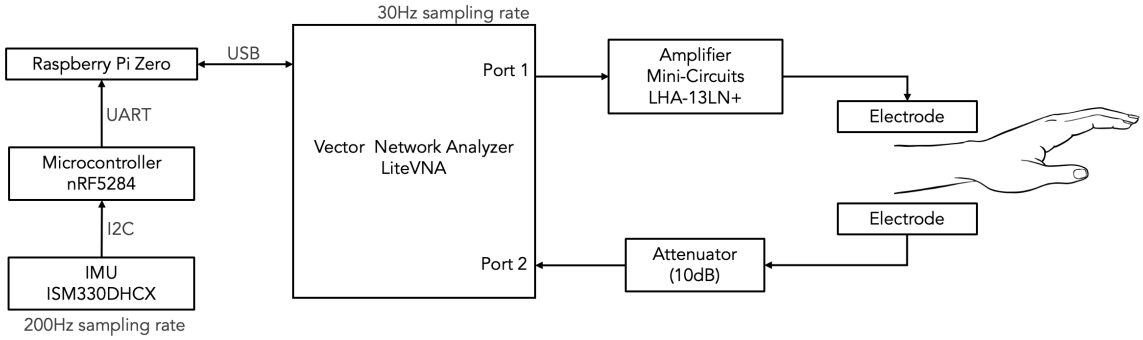
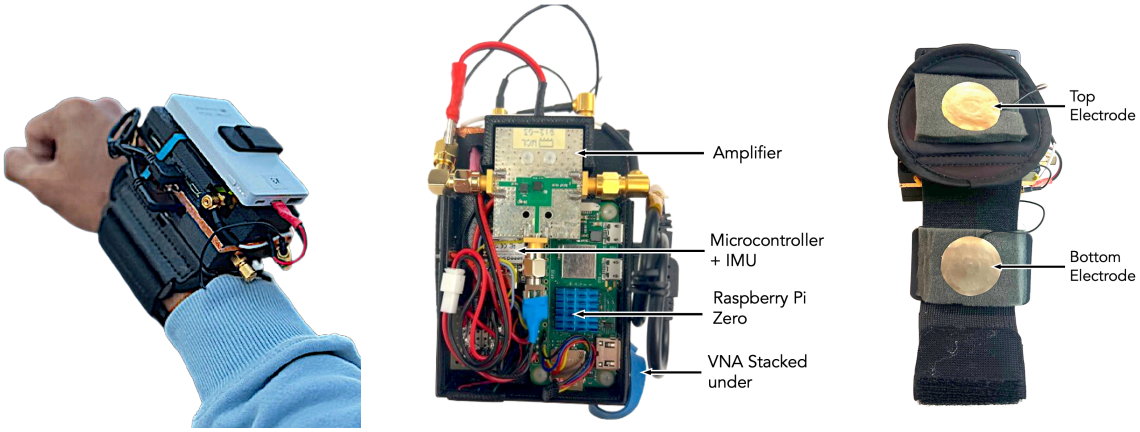


Fig. 10. System architecture of the Z-Band prototype showing hardware components and signal flow. The vector network analyzer (LiteVNA) operates at a 30 Hz sampling rate and interfaces with the amplifier and attenuator for impedance measurement across wrist electrodes. A Raspberry Pi Zero handles data logging and control, while the nRF52840 microcontroller and IMU (ISM330DHCX, 200 Hz sampling rate) provide motion sensing.



(a) The Z-Band prototype worn on the wrist.

(b) Internal structure of the stacked implementation, with the Vector Network Analyzer (VNA) at the bottom, Raspberry Pi Zero, microcontroller, IMU, and amplifier in the middle layer, and the battery (not shown) placed on top.

(c) Bottom view showing the electrode placement and strap mechanism for securing the device on the wrist.

Fig. 11. Z-Band prototype hardware overview.

7 INTERACTIONS

Z-Band supports a range of interactions, including *stateful touch, swipes, taps,* and *pressure-sensitive touch* on external surfaces. Figure 12 illustrates these interactions.

At the core of Z-Band's capabilities is its ability to detect stateful touch, which involves identifying and differentiating between distinct phases of touch interaction, such as touch down, touch hold, and touch release. Unlike tap detection, which captures only momentary contact, stateful touch enables continuous tracking of

touch, forming the foundation for more complex interactions. This capability is crucial for enabling higher-order interactions such as drag-and-drop, scrolling, and drawing, where sustained contact tracking facilitates advanced gesture recognition and interpretation.

Furthermore, Z-Band's sensitivity to contact pressure adds another dimension to its interaction capabilities. This sensitivity stems from how finger pressure alters skin-surface contact, affecting measured impedance. Higher pressure means a larger contact area and a more pronounced impedance change, enabling nuanced pressure-aware input.

Finally, we demonstrate higher-level interactions built on top of stateful touch – swipes and taps – to showcase gestural input. For swipes, the system uses IMU to capture motion; however, this can be extended with other motion-sensitive sensors, such as optical flow sensors, for more advanced gesture tracking. By combining stateful touch, pressure detection, and motion sensing, Z-Band provides a versatile platform for sophisticated interaction design.

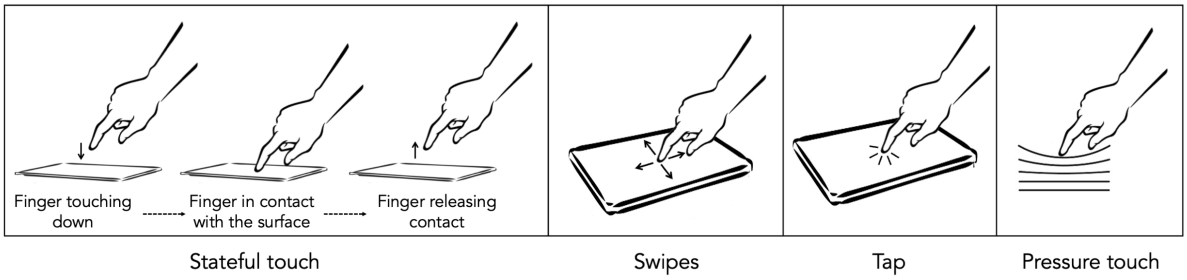


Fig. 12. User interaction types supported by the Z-Band system. The prototype enables detection of stateful touch events (touch down, contact, touch up), as well as dynamic gestures such as swipes, taps, and pressure-based touches performed on everyday, non-instrumented surfaces.

7.1 Stateful Touch

Z-Band combines RF impedance sensing and IMU data for stateful touch detection. While RF impedance sensing provides continuous information about touch-induced signal variations, it is also influenced by hand movement, posing a challenge for touch detection—particularly on dielectric materials that exhibit smaller impedance changes compared to conductive surfaces, making these subtle signals more susceptible to being lost in noise. Figure 9c shows signal changes while touching different materials with the Z-Band prototype.

To address this challenge, we augment our system with IMU data. The IMU, while not sensitive to touch itself, provides valuable information about hand movements and orientation. This motion data helps to disambiguate true touch events from spurious signals caused by hand motion, especially on dielectric surfaces and in dynamic scenarios. Figure 13 shows both RF and IMU data for a touch event in a stationary and walking scenario. By combining the continuous impedance information from RF with the precise motion data from the IMU, Z-Band accurately detects touch-down and touch-up events across a broader range of surfaces and interaction contexts.

7.1.1 Data Processing Pipeline. For real-time touch event recognition, RF and IMU data streams are resampled to 100 Hz. A sliding window of 0.3 seconds scans the data stream to extract features for analysis. When no touch event is detected within the window, it advances with 50% overlap to ensure continuous monitoring. However, when a touch event is detected, the window moves with zero overlap to capture the full event without redundancy.

Feature Extraction from RF Data. A 2D spectrogram, representing both the magnitude and phase of the RF signal, is generated and resized to 224×224 pixels. This resized spectrogram is then fed into a ResNet-51 model for feature extraction. *ResNet-51* is a deep convolutional neural network known for its residual connections, which help train very deep architectures effectively; we use it to extract rich temporal-spatial features from the spectrograms to support accurate touch interaction classification. Instead of using the final classification layer, we extract a 2048-dimensional feature vector from the penultimate layer to serve as the RF feature.

Feature Extraction from IMU Data. Each IMU window is resized to 200 samples. Frequency-domain features, such as FFT, spectral centroid, bandwidth, flatness, and peak frequency, are computed. Statistical features, including mean, median, standard deviation, max, min, variance, and zero-crossing rate, are calculated over 10 equal sub-windows. Additionally, cross-correlation and covariance matrices calculated between IMU axes capture inter-axis relationships.

Feature Fusion and Classification. The RF and IMU feature vectors are flattened and concatenated into a 1-D vector of length 4256, which is passed into a random forest classifier with 300 trees for classification.

7.1.2 Data Augmentation for Robustness. To enhance generalization and robustness, temporal and frequency augmentation are introduced. To account for variability in gesture timing, the RF and IMU data window is shifted up to 0.2 seconds forward and backward in 50 ms steps. To mitigate frequency response variations across users, the RF data is rotated by up to 20 bins along the frequency axis in 5-bin steps in both directions.

7.1.3 Handling Non-interaction Activities. To minimize false positives, a null class is incorporated that includes non-interaction activities such as hand waving, finger movements, arm movements, and stillness. The final classifier is trained to recognize three classes: (1) Touch Down, (2) Touch Up, and (3) Null (No Interaction).

7.2 Pressure Touch

While touching a surface, the user can apply varying pressure levels to trigger distinct touch interactions. The intensity of the press affects the signal transmission between the finger and the surface, altering the signal amplitude. We calculate pressure by summing the amplitude of the S_{21} signal across all frequencies.

The summed amplitude provides a continuous value that is processed through a OneEuroFilter (alpha = 0.01, beta = 0.001) to ensure smooth and stable pressure detection. The filtered pressure values can be scaled to adjust sensitivity and mapped to continuous UI elements, such as sliders or knobs, enabling applications like adjusting speaker volume or screen brightness based on applied pressure.

Figure 15 shows a user gradually increasing pressure (from 0.16N to 4.6N) while interacting with a plastic surface, along with the corresponding summed S_{21} values. The plot reveals a predominantly linear relationship between pressure and summed S_{21} values. By integrating this input modality with real-time feedback and an adaptive UI, Z-Band can enable pressure-sensitive interactions similar to other continuous input techniques explored in prior work [4, 44].

7.3 Swipes and Taps

Z-Band builds on stateful touch detection to enable swipe and tap interactions, supporting four cardinal direction swipes (up, down, left, right) for UI navigation and tap gestures for selection. A state-model-based approach detects these interactions, as shown in Figure 16. Figure 14 shows the sensor raw data while performing swipe interactions.

7.3.1 Tap and Swipe Detection Logic. A *tap* is identified when a touch-up event occurs within 0.2 seconds of a touch-down event. A *swipe* occurs when the duration between touch-down and touch-up falls within the range of

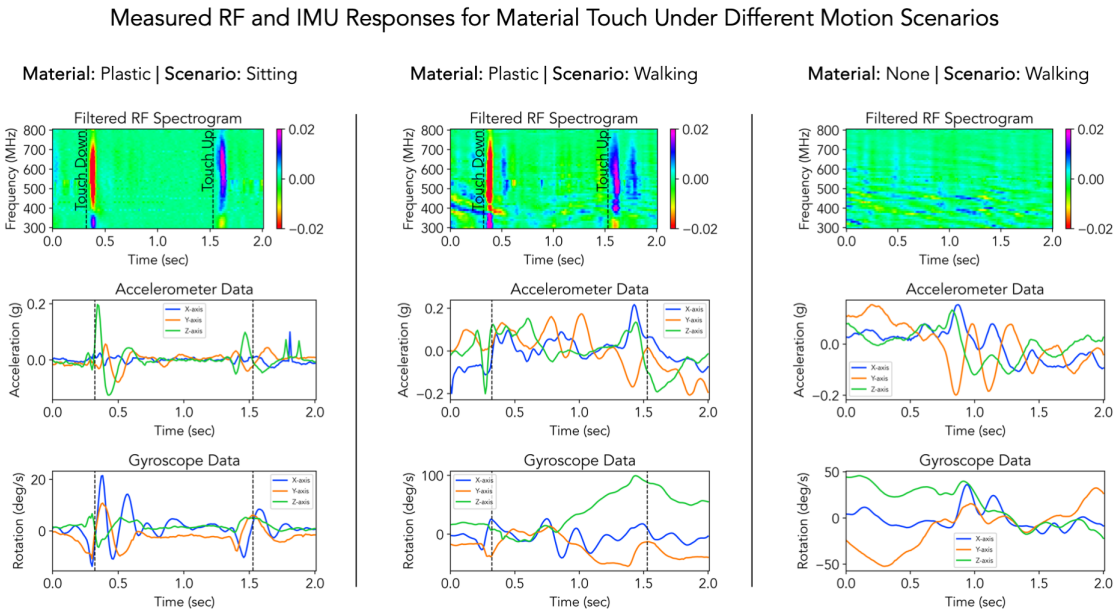


Fig. 13. Measured RF and IMU responses across three motion scenarios. (a) Stationary finger touches on a plastic surface, showing clear touch-down and lift-off events in both RF and IMU data. (b) Walking while touching a plastic surface, where IMU signals exhibit motion-induced noise but RF responses still reveal identifiable touch events.(c) Walking without any surface contact, where motion introduces artifacts but no consistent touch-specific patterns are observed.

0.4 to 1 second. The data captured during this interval is analyzed to determine if a swipe occurred and identify its direction. These time thresholds were empirically determined and can be adjusted for different user preferences.

To improve robustness against incorrectly recognized touch events, we employ an adaptive strategy. For swipe detection, if a touch-up event is not detected within 1 second of a touch down, a 1-second data window following the touch-down event is analyzed to determine if a swipe occurred. Conversely, if a touch-up event occurs without a preceding touch down, a 1-second window before the touch up is evaluated for swipe detection. This approach helps compensate for cases where touch events are missed or incorrectly recognized, ensuring more reliable detection of swipe interactions. As mentioned in Section 8.4, this method effectively captures swipes while minimizing false positives.

7.3.2 Swipe Direction Recognition. For swipe direction classification, we employ a machine learning-based approach similar to tap detection but with a reduced feature set to improve surface-agnostic recognition. RF data is excluded to prevent surface characteristics from influencing the model, ensuring consistent swipe recognition across different surfaces. Additionally, frequency-based IMU features are omitted to reduce the potential impact of surface texture variations, focusing instead on statistical IMU features for classification. To further improve robustness, time-domain data augmentation techniques—similar to those used for touch-up and touch-down detection—are applied. The final classification is performed using a random forest model with 300 trees, leveraging only statistical IMU features for swipe direction recognition.

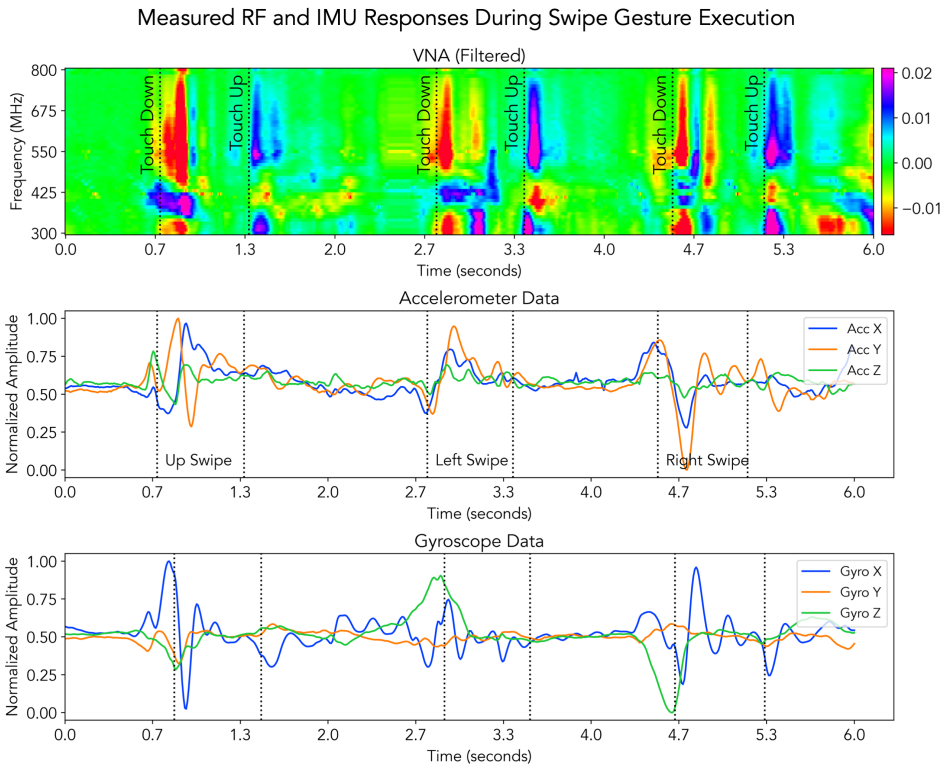


Fig. 14. Measured RF and IMU responses during the execution of three swipe gestures. The vertical dotted lines on the VNA spectrogram mark the detected touch-down and lift-off points identified by the touch detection model. The corresponding swipe directions (ground truth) are indicated on the accelerometer plots.

7.4 Putting It All Together

To create a complete user interface, all user interactions—stateful touch, swipes, taps, and pressure touch—must work seamlessly in tandem. We adopt a *state-based model* to govern interaction flow in Z-Band, enabling transitions between touch down, pressure touch, swipes, and taps. This design prioritizes interpretability, offers low latency for real-time interaction, ensures stability across users without requiring retraining, and provides practicality for always-on wearable systems where computational resources are limited. While machine learning–based state transitions hold promise for more adaptive and scalable interaction modeling with growing datasets, our early evaluations showed that a rule-driven approach offered greater reliability given the modest size and diversity of our current dataset.

In Z-Band's interaction state-model, when a touch-down event occurs, the system determines the appropriate interaction mode based on the detected motion and timing. If the touch down is not followed by significant IMU motion within 0.2 seconds, the system activates pressure touch mode. Significant IMU motion is identified by analyzing motion magnitude from the IMU data, with thresholds empirically established through testing and data collection. In pressure touch mode, users can vary the pressure applied to the surface, producing a continuous pressure value. The mode exits when a touch-up event is detected or after five seconds have elapsed, ensuring interactions remain intuitive and time-bound.

In contrast, when significant IMU motion is detected within 0.2 seconds of a touch down, the system transitions to swipe and tap detection mode, as detailed in Section 7.3. This ensures that dynamic gestures, like swipes and taps, are accurately recognized without interfering with static, pressure-based interactions.

This interaction logic is shown in Figure 16, illustrating the transitions between pressure touch, swipe, and tap states. By leveraging this structured approach, Z-Band ensures seamless and reliable recognition of user interactions across various contexts.

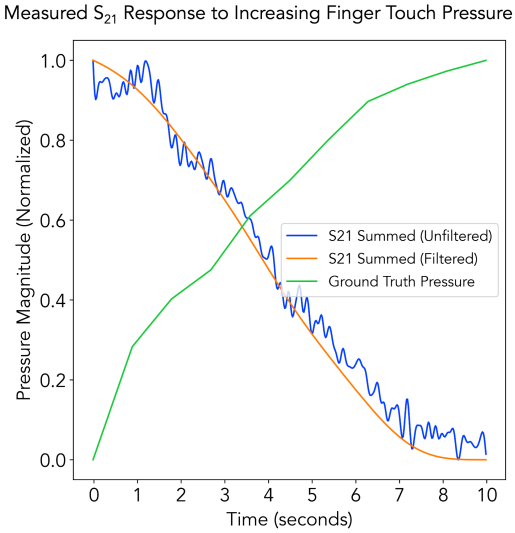


Fig. 15. Summed S_{21} magnitude response to increasing pressure (from 0.16N to 4.6N), showing both unfiltered and filtered data alongside ground truth pressure measurements.

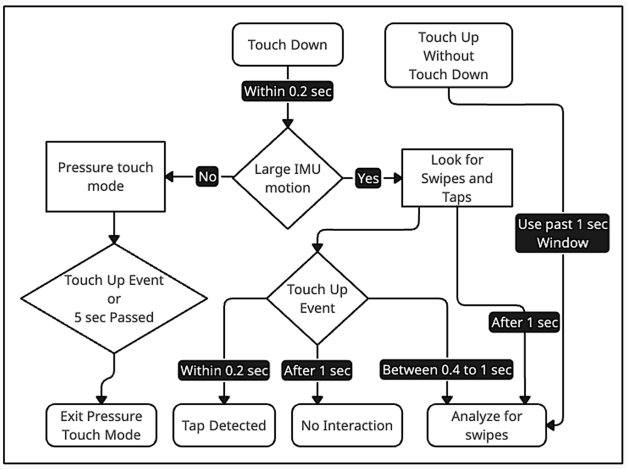


Fig. 16. Interaction flow diagram for the Z-Band system, illustrating the detection logic for touch, swipe, and pressure-based interactions.

8 USER EVALUATIONS AND RESULTS

We evaluated Z-Band to assess its performance across various interactions, participants, and scenarios. Our evaluation focused on characterizing the system's performance under practical conditions, including natural interaction variability and after-device wear/removal.

We conducted four distinct studies:

(1) **Stateful Touch Study**: To evaluate the system's ability to detect and differentiate stateful touch interactions (touch down, touch up) across different participants and surfaces.
(2) **Touch Sensitivity Study**: To examine the system's performance, detecting interactions with varying pressure levels.
(3) **Swipe Gesture Study**: To assess how accurately the system recognizes swipe gestures.
(4) **False Positive Study**: To analyze the frequency of false positives in scenarios without intentional interactions.
(5) **Electrode Material Study**: To compare the performance of different electrode materials in terms of signal quality.

(6) **False Positive Study**: To analyze the frequency of false positives in scenarios without intentional interactions.

During the studies, participants performed a predefined set of interactions, which we define as a *session*. After completing each session, participants took a short break and were instructed to remove and re-wear the prototype device. This intentional repositioning introduced natural variation in electrode placement across sessions, simulating real-world conditions where wearables are not always worn identically. Such variability affects signal quality due to shifts in contact area and impedance baselines. Additionally, we observed minor changes in skin moisture through sweat accumulation over time, which also influenced signal consistency. By capturing data across these variations, we trained and evaluated our system under more realistic and diverse usage scenarios, improving its generalizability and robustness. We sanitized the device and electrodes thoroughly after each participant to maintain hygiene.

Our user study, approved by the Institutional Review Board (IRB), involved 16 participants (10 female and 6 male) recruited from our university. Participants were university students between the ages of 18 and 40. Each received a 30 USD gift card as compensation for their time. The study took approximately 60 minutes for each participant to complete.

8.1 Data Collection Tool

To facilitate accurate and consistent data collection, we developed a custom user interface (UI) inspired by the 'Guitar Hero' style interface. This UI provided dynamic visual cues to guide users through specific interactions at designated times and durations, as shown in Figure 17.

The interface features floating rectangles, each representing a distinct interaction. The length of a rectangle corresponds to the allocated time window for that action. The rectangles move across the screen, and users are prompted to perform the action when a rectangle intersects a vertical line, signifying its active state. Clear text labels beside each rectangle specify the action to be performed (e.g., "Tap," "Swipe," "Hold").

This dynamic design offers several advantages for data collection and analysis. The moving bar and rectangle intersections provide clear visual cues for the start and end times of each interaction, *ensuring precise timing and synchronization*. The speed of the moving bar can be adjusted, allowing for *customizable pacing of interactions* to accommodate different user needs and data collection requirements. Additionally, the *interface presents a preview of upcoming actions*, enabling users to anticipate and prepare for interactions in advance. Beyond guiding user input, the rectangle windows *function as a ground truth annotation tool*, automatically marking the exact start and end times of interactions. This ensures accurate segmentation of sensor data, facilitating reliable analysis and effective model training.

This tool streamlines data collection and ensures consistency by providing clear visual guidance and precise timing information. This enhances the reliability and quality of the collected data, which is crucial for developing robust interaction models.

8.2 Study 1: Evaluating Stateful Touch Detection

This study evaluates Z-Band's ability to accurately detect touch-down and touch-up events across different materials and movement conditions. The goal is to assess its robustness for real-world applications, ensuring reliable performance across diverse surfaces and usage scenarios.

8.2.1 Factors Affecting the Experiment.

Influence of Material Conductivity. Material conductivity significantly impacts impedance sensing. Conductive materials, such as metals, generate strong signal variations, whereas dielectric materials, such as plastic and

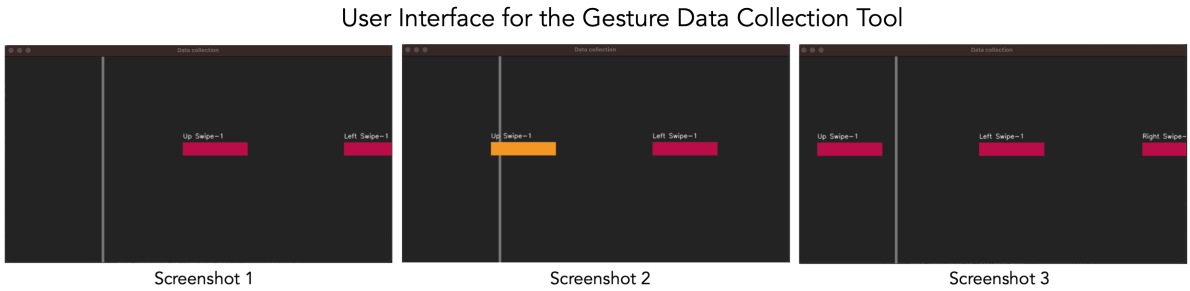


Fig. 17. Three snapshots of the data collection UI at various points in time. (1) The next action for the user to perform is an "Up Swipe," followed by a "Left Swipe." (2) The "Up Swipe" action window is active (highlighted in yellow), prompting the user to perform the gesture. (3) The "Up Swipe" action window has concluded, and the upcoming actions are "Left Swipe" followed by "Right Swipe."

wood, produce weaker changes. To evaluate performance across a range of conductivities, we selected five test materials: plastic (low), wood (low), cotton cloth (medium), human palm (medium), and copper (high).

Impact of Motion and Movement. Since our system incorporates an IMU and skin-worn electrodes, motion can impact its performance by introducing artifacts into IMU data and noise into the RF sensor readings due to electrode shifts on the skin. To assess the impact of this, we evaluated Z-Band's performance in both stationary (sitting) and dynamic (walking) scenarios. The system's wireless and battery-powered design enabled seamless data collection during walking scenarios.

8.2.2 Study Protocol. To evaluate our system's performance, participants were instructed to perform touch-down and touch-up actions on the five different materials (plastic, wood, cotton cloth, copper, and human palm) with a 2-second gap between actions, as displayed on a screen using our custom data collection tool. Each participant completed ten sessions, with each session involving five touch events on each material. To ensure diverse data and prevent over-fitting to specific device orientations or electrode placements, the wristband prototype was removed and re-worn after each session. Data collection occurred under two conditions: stationary (seated) for the first four sessions and dynamic (walking) for the remaining six. This procedure helped us assess the impact of both material properties and motion on touch detection accuracy.

In addition to touch-up and touch-down events, we also recorded data for non-interactive motions (null), like finger movement, arm movement, and stillness, in both sitting and walking scenarios. This data is essential for training the system to differentiate between intentional user interactions and incidental motions, thereby filtering out false positives and preventing the system from misinterpreting incidental motions as intentional touch interactions. The null data collected in this study was also used in subsequent studies we conducted in this paper.

8.2.3 Model Training. We aim to design a system that generalizes across users and interaction surfaces, eliminating the need for per-user or per-surface calibration in real-world use. To this end, we trained a *single, unified model* using data from multiple surface types—wood, plastic, copper, glass, and skin—so the model can generalize across material properties without retraining. This model treats surface material as a source of natural variability, allowing it to learn generalizable features for touch segmentation regardless of the specific surface. We combined touch-down and touch-up data across all surfaces and treated them as a unified class to create a comprehensive dataset for model training (see Section 7.1 for feature extraction details).

In addition to cross-surface generalizability, we aim for *user-independent deployment.* Therefore, our final reported results are based on *user-independent models* trained using leave-one-user-out cross-validation (LOOCV). For each fold, we trained the model on data from all but one participant and evaluated it on the held-out user's data. This approach ensures that the model has never seen any data from the test user, simulating deployment to a new, unseen user without fine-tuning or calibration.

We also evaluated models trained under narrower conditions not as our primary approach, but to provide further insights for readers who may wish to tailor the system to specific scenarios—such as stationary or mobile use—for optimized performance in their intended context. These conditions include models trained only on sitting or walking data, as well as user-dependent models that reflect scenarios where users may choose to fine-tune the system to their own data. For user-dependent evaluation, we trained on all but one session from a participant and tested on the remaining session, simulating cross-session generalization. Importantly, no user-dependent models were trained and tested on data from the same device wear session, ensuring that performance reflects robustness to repositioning and real-world variation.

Our model includes three classes: touch-down, touch-up, and a null class representing incidental or non-intentional actions. To create the null class, we recorded continuous non-interaction movements (approximately 5 minutes per user), which are much longer than typical interaction events (1 second). We segmented this continuous data into 1-second windows to generate comparable null samples using a sliding window with 50% overlap. Since the null class is overrepresented, we applied random upsampling to the touch-down and touch-up classes to balance the dataset. We applied this preprocessing strategy consistently across all models and evaluations to ensure balanced training and fair comparison.

Together, these analyses provide a comprehensive view of Z-Band's generalization capacity across users, surfaces, and usage scenarios. Our findings, discussed in the next section, suggest that while tailored models can offer incremental improvements in specific contexts, our unified user-independent model already achieves robust performance without requiring per-user calibration or surface-specific tuning.

8.2.4 Results. In stationary (sitting) scenarios, both user-dependent and user-independent models achieved over 95% accuracy, with the user-dependent model reaching the highest accuracy of 97% across all scenarios. The sitting condition consistently outperformed the walking condition, likely due to the motion-induced noise affecting both RF and IMU signals. The lowest accuracy was observed in the walking scenario with the user-independent model, at 89.6%, while all other scenarios maintained accuracy around 90%. Notably, touch-down and touch-up accuracy remained above 90% across all scenarios. However, during walking, null detection accuracy declined for the user-independent model scenario, indicating a higher likelihood of false positives. Expanding the dataset with additional non-interaction scenarios could help mitigate false positives and improve classification robustness. Figure 18 presents the confusion matrices for all scenarios.

8.2.5 Sensor Ablation Analysis. The previous section examined the combined impact of bio-impedance and IMU sensing on surface interactions across different materials and scenarios. Here, we conduct an ablation study to quantify the individual contributions of each sensor modality to overall system performance, crucial for understanding the relative importance of each sensor, identifying potential areas for optimization, and informing future design decisions regarding sensor selection and fusion strategies.

Figure 19 presents Z-Band's overall performance using IMU alone, RF alone, and the combined IMU+RF approach, while Figure 20 presents corresponding confusion matrices for the user-independent IMU-only and RF-only models.

Across all conditions, the combined RF+IMU model consistently outperformed the single-modality baselines, highlighting the complementary nature of the two sensors and mutually reinforcing benefits. This benefit was particularly evident in the walking condition, where motion artifacts degrade individual sensor performance more significantly. For example, IMU-only performance dropped to 71% during walking, while RF-only maintained a

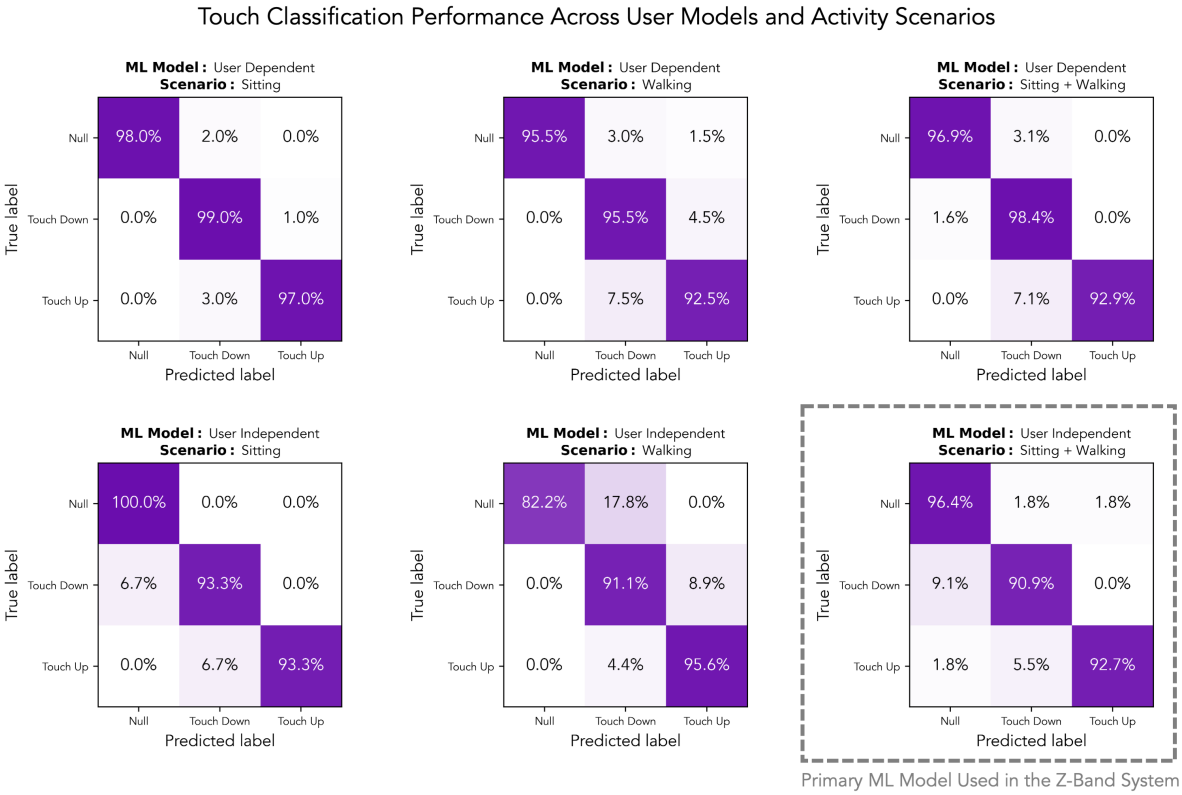


Fig. 18. Touch classification performance across user-dependent and user-independent ML models using combined RF and IMU data for sitting, walking, and combined activity scenarios. The user-independent model trained on both sitting and walking data (highlighted) represents the primary ML model used in the Z-Band system.

slightly higher 79%. When combined, however, the system achieved up to 90% accuracy, demonstrating that RF helps mitigate IMU noise, and vice versa.

The confusion matrices (Figure 20) offer deeper insight into the classification behavior of each modality. RF-only models showed stronger performance in distinguishing touch states, especially touch up and touch down, during sitting. IMU-only models were more affected by motion-related confusion, particularly in walking scenarios, where both touch classes were misclassified more frequently. These patterns suggest that while RF provides more stable absolute signal features, IMU data captures dynamic changes—making their combination well-suited for robust interaction detection.

8.2.6 Computational Performance and Optimization. For easier prototyping, all code and inference were run on a MacBook M2 laptop. The data pipeline for a single inference cycle had a latency of 20 ms to fetch data, 2 ms for IMU feature calculation, 80 ms for ResNet-51 inference, and 10 ms for the Random Forest classifier. This resulted in a total latency of approximately 112 ms, with the majority of the time being consumed by the ResNet-51 model.

The ResNet-51 model was initially chosen for its high accuracy, which allowed us to test the full potential of the system. However, as a large model, it demands significant computational resources, which can be a limitation

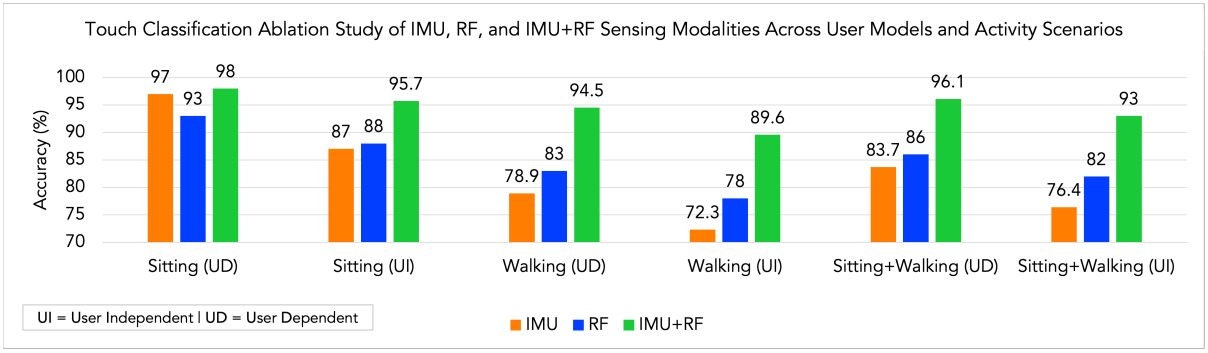


Fig. 19. Ablation study of sensor modality performance for touch classification across sitting, walking, and combined activity scenarios, using IMU-only, RF-only, and combined IMU+RF sensing for user-dependent (UD) and user-independent (UI) models.

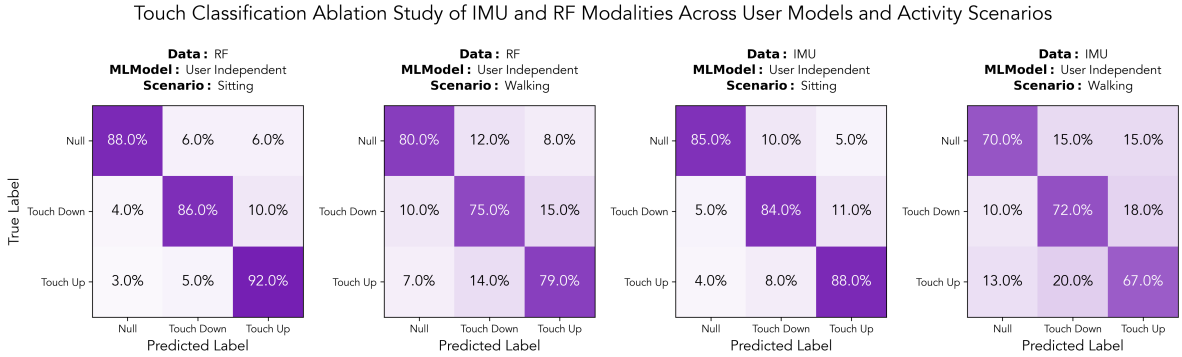


Fig. 20. Tap force classification accuracy across user-dependent (UD) and user-independent (UI) models using IMU, RF, and combined IMU+RF sensing modalities for soft, regular, and hard tap interactions.

for real-time applications on edge devices. To address this, we explored an alternative by using the MobileNetV2 model for feature extraction; MobileNetV2 is a lightweight architecture optimized for mobile and embedded vision applications. By substituting ResNet-51 with MobileNetV2, we significantly reduced the inference time for the feature extraction step to just 20 ms. This brought the total system latency down to 52 ms, a reduction of over 50%. This computational efficiency can be further optimized through dedicated software optimizations and hardware acceleration.

While there was a slight drop in accuracy with the MobileNetV2 model, the performance remained high. With the ResNet-51 model, the user-independent accuracy was 89.6% for walking, 95.7% for sitting, and 93.0% for the combined sitting and walking activity. In comparison, the MobileNetV2 model achieved a user-independent accuracy of 83.2% for walking, 92.7% for sitting, and 87.8% for the combined sitting and walking activity. These results demonstrate a clear path towards the practical deployment of this technique on resource-constrained edge devices, balancing high performance with the demands of real-time operation.

8.3 Study #2: Evaluating Sensitivity to Touch Pressure

Combining bio-impedance sensing with IMU data enables the detection of subtle touch interactions, outperforming IMU-only approaches. This increased sensitivity is due to the active broadband nature of our impedance sensing, which captures even minor variations in touch pressure.

We evaluated Z-Band's touch sensitivity by conducting a user study with five participants, each performing three distinct tap interactions—soft, regular, and hard—on a plastic surface. Taps were chosen over touch-down and touch-up events because they provide a single, well-defined force application. In contrast, maintaining consistent force during sustained contact (as in touch down and touch up) proved challenging in a pilot study, leading to significant user variability. By using taps, we minimized this variability and ensured that each interaction produced a distinct and controlled force measurement, improving the reliability of our analysis.

8.3.1 Study Protocol. In this study, participants performed three types of taps on a plastic surface: soft, regular, and hard. The plastic surface was mounted on a sensitive weight scale to provide ground truth force measurements for each tap. Each participant performed 10 repetitions for each of the three tap types, resulting in a total of 30 taps per participant.

8.3.2 Model Training. During the study, RF and IMU data were collected synchronously. The data was processed using the feature extraction pipeline described in Section 7.1. Tap detection and classification were performed using a Random Forest classifier (number of trees = 300). For the user-independent model, we used leave-one-user-out cross-validation (LOOCV), iteratively training on all but one participant and testing on the held-out user. To quantify the extent to which user calibration can improve system performance, we additionally trained user-dependent models tailored to individual participants. For user-dependent analysis, we adopted a stratified approach, utilizing approximately 70% of each user's data for training and the remaining 30% for testing. The user-independent analysis employed LOOCV.

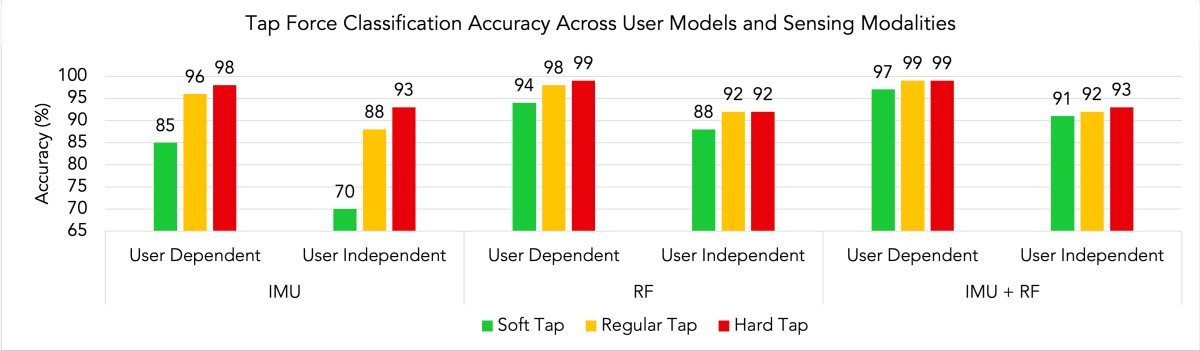


Fig. 21. The comparative performance of IMU, RF, and their combination for classifying three tap types, i.e., soft, regular, and hard, in both user-dependent (UD) and user-independent (UI) scenarios.

8.3.3 Results. We developed models using IMU-only, RF-only, and combined IMU+RF inputs, with the results shown in Figure 21. The average forces applied for soft, regular, and hard taps were 0.18N, 0.48N, and 1.63N, respectively, as measured by the weighing scale across all participants.

The *IMU-only model* struggled with detecting soft taps, achieving 85% accuracy in the user dependent (UD) scenario and dropping to 70% in the user independent (UI) scenario, indicating its limitations in capturing subtle,

low-pressure interactions. However, it performed better for regular and hard taps, with accuracies up to 98% in the UD and 93% in the UI cases since these taps generate more pronounced motion signals.

In contrast, the *RF-only model* performed better at detecting soft taps, achieving 94% accuracy in the UD scenario and 88% in the UI scenario, demonstrating its sensitivity to subtle pressure changes. For regular and hard taps, the RF model delivered consistently high accuracy, comparable to or slightly exceeding the IMU's performance.

The *combination of IMU and RF* data provided the best overall results, significantly improving soft tap detection to 97% in the UD and 91% in the UI scenarios, while achieving near-perfect accuracy (up to 99%) for regular and hard taps. These results underscore the critical role of RF sensing in enhancing sensitivity to subtle touches. They also highlight the robustness achieved through the fusion of IMU and RF data, making the system highly reliable across all touch types and user scenarios.

8.4 Study #3: Evaluating Swipe Gesture Recognition

This study evaluates swipe gestures performed on a plastic surface. Plastic, with its low conductivity, presents a challenging scenario for impedance-based touch sensing, allowing us to assess the robustness and sensitivity of our approach in a more demanding context.

8.4.1 Study Protocol. Sixteen participants were instructed to perform four directional swipes (left, right, up, down), each performed within a 1-second window. Each participant completed four sessions, performing five repetitions of each swipe direction per session. After each session, the Z-Band prototype was removed and re-worn to capture data from different device orientations and electrode placements. All sessions were conducted with participants in a seated position.

8.4.2 Model Training. We conducted a two-part evaluation of swipe gesture recognition.

(1) **Swipe Detection Accuracy**. First, we assessed the accuracy of swipe recognition using segmented swipe data based on ground truth labels collected during the study. This let us evaluate the performance of the gesture recognition model in isolation.
(2) **Swipe Segmentation in Continuous Data**. Next, we evaluated the system's ability to segment swipe gestures within a continuous data stream. This involved using a stateful touch detection model (trained on data from all users in the sitting scenario from the previous study) to identify potential swipe gestures and then evaluating the accuracy of classifying those segmented gestures. This approach provides a more realistic assessment of the system's performance in a real-world scenario.

For both swipe detection and segmentation evaluations, we developed user-dependent and user-independent models using the IMU data and a Random Forest classifier (see Section 7.3 for feature extraction details). LOOCV was employed for model evaluation.

8.4.3 Results.

Swipe Classification Accuracy. Using ground truth swipe data windows, both user-dependent and user-independent models achieved high accuracy in classifying left, right, up, down, and null gestures. User-dependent models achieved an impressive average accuracy exceeding 96%, with a range of 96% to 100%. The user-independent model also performed well, with an average accuracy of 93%, ranging from 92.3% to 100%.

Swipe Segmentation Performance. In evaluating swipe segmentation, 74% of swipes had both touch up and touch down correctly detected, while 11% had only one of these events correctly identified. In 10% of cases, a single event was detected but misclassified (e.g., touch-up mistaken for touch-down), and 5% were not detected at all. To address cases where touch events were missed, we applied an adaptive correction strategy: for touch-up events without a preceding touch down, a 1-second window before the touch up was analyzed, and for touch-down

events without a following touch up within 1 second, a 1-second window after the touch down was included for evaluation.

Additionally, we detected extra touch-up/down events that did not correspond to actual swipes. These spurious events, which constituted 4% of the total detected touch events, were included in the testing dataset to evaluate the robustness of the swipe detection model in handling spurious touch events and filtering out false positives.

Swipe Classification Accuracy in a Continuous Data Stream. For swipe classification, a model was trained using ground-truth-segmented data, while the test data was segmented using the touch detection model to simulate real-world performance. The classification model achieved 94.2% accuracy in user-dependent cases and 91.4% in user-independent cases. Importantly, non-swipe windows mistakenly segmented by the touch detection model were correctly classified as null, demonstrating the system's strong false-positive rejection and reliable real-world swipe recognition.

8.5 Study #4: Analyzing False Positives

In human-computer interaction (HCI) research, minimizing false positives is crucial for creating seamless and reliable user experiences. A high rate of false positives—where the system mistakenly detects a gesture or interaction—can lead to frustration, reduce user trust, and ultimately degrade the interface's usability. To evaluate and minimize false positives, we used the data collected from a previous study and performed an evaluation.

8.5.1 Methodology. To evaluate false positive rates, we applied the touch-up/down and swipe recognition models trained in previous studies to a continuous stream of null test data, totaling 80 minutes, collected from earlier experiments. We used a sliding window approach to detect touch events, with a 0.2-second window and 50% overlap. When a touch-up or touch-down event was detected, the overlap was set to 0 to prevent redundant detections. Using this approach, all touch-up and touch-down events in the null dataset were identified, and their occurrences were analyzed to assess false positive rates.

Following this, we applied gesture detection to the detected touch events to further analyze false positive performance at the gesture level. Temporal constraints were imposed to ensure only valid gestures were recognized: taps were required to be shorter than 0.2 seconds, swipes had to fall within the 0.4 to 1-second range, and any window considered for a swipe was further processed through the swipe recognition model to confirm its validity.

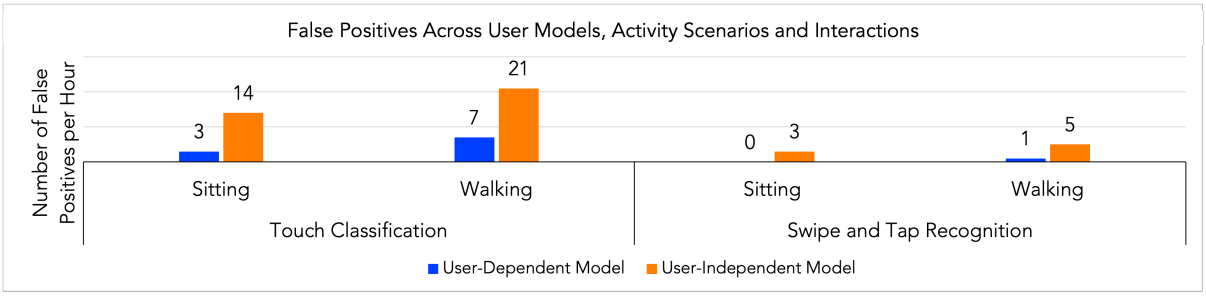


Fig. 22. False positives per hour for two interaction layers—basic touch classification (touch-up/down events) and higher-level gesture recognition (taps and swipes)—under sitting and walking conditions, showing a reduction in false positives when gesture recognition is applied over basic touch detection.

8.5.2 Results and Analysis. Figure 22 presents the false positive rates for both user-dependent and user-independent models in different scenarios. As expected, the false positive rates were higher during walking compared to

sitting, likely due to the increased motion artifacts affecting both IMU and RF data. The user-independent models also exhibited higher false positive rates than the user-dependent ones, reflecting the challenge of generalizing across users.

Crucially, applying the temporal and gesture-specific constraints significantly reduced false positives. In the sitting scenario, the user-dependent model achieved a 0 false positive rate per hour for gesture recognition, while the user-independent model's rate was reduced to 3 per hour. This highlights the effectiveness of incorporating higher level knowledge and constraints to improve system robustness.

These results demonstrate that while Z-Band's basic touch detection exhibits some false positives, these can be effectively mitigated by incorporating constraints and more complex patterns. This multi-layered approach enhances the reliability of the system and paves the way for practical and user-friendly touch and gesture interfaces. Future work can explore additional strategies for minimizing false positives, such as adaptive thresholds and personalized calibration, to further improve the robustness of Z-Band in diverse real-world scenarios.

8.6 Study #5: Effect of Skin Moisture

To investigate how skin moisture and electrode composition affect the performance of our impedance sensing system, we conducted a supplementary evaluation involving three participants. The study aimed to assess both signal characteristics and classification performance under variations in skin hydration.

8.6.1 Protocol. To simulate skin moisture, participants were instructed to apply a damp towel to their wrist before each trial to match the skin condition observed immediately after hand washing. Each participant performed a series of tap gestures under both *dry* and *moist* skin conditions.

We recorded impedance signals in both *touch* and *no-touch* states using the system's original gold-coated copper electrodes. The measurement setup remained identical to the main evaluation (section 8.2), with the same frequency sweep range (300-800 MHz) and electrode configuration (15 mm radius), ensuring consistency and isolating the effect of skin moisture as the only experimental variable. Participants touched two different surface types during the trials: *wood* (non-conductive) and *copper* (conductive). Each participant performed 20 repetitions per condition (dry/moist) (2 skin conditions × 2 surfaces × 20 repetitions = 80 trials per participant), yielding a total of 240 interaction samples across three participants.

Beyond raw signal analysis, we also evaluated system robustness to moisture by running inference on the data from this study using a classifier that was trained only on dry-skin trials from Study #1. This setup allowed us to simulate a real-world generalization scenario, where the system must operate under varying skin conditions without per-user calibration.

Table 4. Maximum Signal change (in dB) between touch and no-touch conditions across different skin moisture levels, showing reduced signal magnitude under moist skin conditions compared to dry skin.

Surface	Skin Condition	Maximum Signal Change (dB)
Wood	Dry	0.06
	Moist	0.03
Copper	Dry	0.23
	Moist	0.11

8.6.2 Results. As shown in Table 4, skin moisture consistently reduced the touch-induced signal change across both surface types. For the wood surface, the impedance change dropped from 0.06 dB (dry) to 0.03 dB (moist), while on copper it decreased from 0.23 dB to 0.11 dB. Although moisture improves skin-electrode conductivity by reducing contact impedance, this lower baseline impedance causes the additional conductive path through the touched surface to represent a smaller relative change. Consequently, the differential between touch and no-touch conditions decreases, reducing overall touch sensitivity despite improved electrode coupling.

Despite this reduction in physical signal magnitude, the system maintained high classification performance. Using a user-independent model trained only on dry-skin data, we observed a touch classification accuracy of 96.9% (dry) and 96.5% (moist) on copper, and 92.0% (dry) versus 91.1% (moist) on wood. These results suggest that while absolute signal deltas are smaller under moist conditions, the model remains robust due to the discriminative features captured in the RF and IMU data.

Overall, this evaluation demonstrates that Z-Band can generalize well across different skin conditions and maintain reliable performance even under varied moisture scenarios without retraining or recalibration.

8.7 Study #6: Effect of Electrode Materials

To explore alternatives to our original gold-coated copper electrodes, which are highly conductive but not suitable for wearable textiles, we evaluated two conductive fabrics with three participants. The goal was to find a material that could be seamlessly integrated into clothing while still providing reliable signal acquisition.

The two fabrics tested were:

(1) **Knit Jersey Conductive Fabric**: Composed of 63% cotton, 35% silver yarn, and 2% spandex. Its key properties are high flexibility and comfort, making it well-suited for wearables.
(2) **Woven Conductive Fabric**: Made of approximately 70% polyester, 16% copper, and 14% nickel. This material is less flexible and conforms less readily to skin contours due to its tight weave. However, its dense metal content gives it superior conductivity compared to the knit fabric.

8.7.1 Protocol. We fabricated electrodes from the two conductive fabrics (knit jersey and woven conductive fabric) with the same geometry as our gold-coated copper electrodes (15 mm radius). The measurement setup remained identical to Section 8.2 (300-800 MHz frequency sweep, same amplification settings), isolating electrode material as the only experimental variable.

For each electrode material, we measured impedance under two conditions: *no-touch* (hand in air) and *touch* (hand touching a surface). Two surfaces were tested—*wood* (non-conductive) and *copper* (conductive)—to assess signal sensitivity across different electrical properties. Three participants each performed 10 repetitions per electrode-surface combination (3 electrode types × 2 surfaces × 10 repetitions = 60 trials per participant), yielding 180 total trials.

To evaluate cross-material generalization, we applied the touch classifier trained on gold-coated copper electrode data (Study #1) to the fabric electrode data without retraining.

8.7.2 Results. Table 5 shows that electrode material significantly affects touch detection sensitivity. Gold-coated copper electrodes achieved the highest signal changes, outperforming knit jersey fabric and woven conductive fabric. The superior performance of gold-coated copper stems from its low contact impedance, high conductivity, and stable skin interface with minimal oxidation. Fabric electrodes exhibit lower sensitivity due to their porous structure creating inconsistent skin contact, higher bulk resistivity, and air gaps at the electrode-skin interface. Knit fabric outperforms woven fabric owing to better conformability and skin contact. This reveals a fundamental trade-off: metal electrodes maximize sensing performance but may compromise comfort, while fabric electrodes prioritize wearability at the cost of reduced sensitivity.

Table 5. Maximum Signal change (in dB) between touch and no-touch conditions for different electrode types, showing that metal-based electrodes (e.g., gold-coated copper) produce higher signal variations compared to fabric-based electrodes.

Electrode Type	Surface	Maximum Signal Change (dB)
Gold-Coated Copper	Wood	0.07
	Copper	0.21
Knit Jersey Fabric	Wood	0.03
	Copper	0.08
Woven Conductive Fabric	Wood	0.01
	Copper	0.06

When we applied the pre-trained classifier to the new data, we observed a performance drop. For Knit Jersey Fabric, the user-independent classifier achieved 83.2% accuracy on copper and 68.0% on wood. For Woven Conductive Fabric, the accuracy was 79.4% on copper and 55.2% on wood. The degradation in performance was more significant on non-conductive surfaces, where the signal margins are already narrow. This highlights the critical need to either train or fine-tune models specifically for the electrode material being used to maintain high accuracy.

After adding the small number of samples (5 per class) from each of the new electrode materials to the training set, the classification accuracies improved significantly. For Knit Jersey Fabric, the user-independent accuracy increased to 87.8% on copper and 81.1% on wood. For Woven Conductive Fabric, the model reached 93.5% on copper and 75.3% on wood.These results indicate that while material choice directly impacts signal quality and model performance, a small amount of fine-tuning can effectively adapt a model to new electrode types and restore higher classification accuracy.

9 Z-BAND LITE: A COMPACT AND LIGHTWEIGHT PROTOTYPE

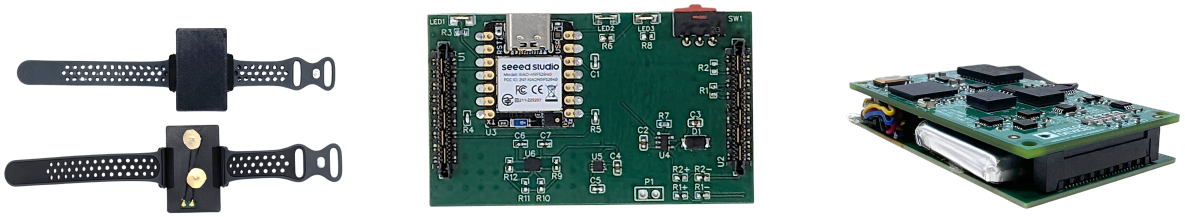
The Z-Band prototype used for evaluation offered significant advantages, including large bandwidth and amplified transmission power, allowing us to test the system under challenging conditions. However, its complex hardware setup, which included a full VNA and a Raspberry Pi computer, made the device bulky and less practical for everyday use.

In this section, we introduce Z-Band Lite, a compact, lightweight, and wearable alternative that remains effective for core interaction tasks. This prototype measures 70 x 60 x 20 mm and weighs about 90 gms. Figures 1(B) and 23a show this prototype.

9.1 Hardware Design and Components

At the heart of Z-Band Lite is the ADMX2001B impedance analyzer measurement module from Analog Devices. Measuring only 63mm x 38mm, this module supports impedance measurements from 0.2 Hz to 10 MHz. It operates at 3.3V and offers UART and SPI interfaces, making it ideal for miniaturized designs.

Although the ADMX2001B module comes with an evaluation board (EVAL-ADMX2001EBZ) for testing and connections, its large size (150mm x 200mm) makes it unsuitable for our wearable application. To address this, we developed a custom expansion board matching the size of the ADMX2001B module. This custom board, shown in Figure 23b, stacks directly below the ADMX2001B module (Figure 23c) and houses an ESP32 microcontroller, an



(a) Z-Band Lite Prototype: Top and bottom views.

(b) Custom expansion board for ADMX2001B.

(c) Stacked PCB assembly of the complete Z-Band Lite system

Fig. 23. Visual overview of the Z-Band Lite prototype and hardware components.

ISM330DHCX IMU, and a battery charger for the onboard 400mAh battery. The prototype is entirely wireless, with the microcontroller transmitting impedance and IMU data seamlessly over WiFi.

The electronics are encased in a 3D-printed housing, with a repurposed Apple Watch wristband used to secure the device on the wrist. Two gold-coated electrodes, each 20mm in diameter, are attached to the bottom of the case to ensure stable skin contact for impedance measurements. The prototype consumes about 300 mA of current at 3.3V.

9.2 Functional Capabilities and Limitations

The Z-Band Lite prototype operates within a 1–10 MHz frequency range. While its narrower bandwidth and lower transmission power than the original Z-Band prototype reduces sensing capability, it excels at detecting touch on medium- to high-conductivity surfaces, such as human skin and metals. This capability makes it particularly well-suited for on-body interactions, like using one hand to interact with the palm of the other, as shown in Figure 1 (D).

The reduced capabilities of Z-Band Lite are not inherent to its compact form factor but rather a result of using off-the-shelf hardware. This smaller functional Z-Band Lite prototype already demonstrates a promising path toward miniaturization and adds confidence in the feasibility of our sensing approach. Further size and hardware optimizations remain possible through integrated circuit design and custom packaging. With custom-designed hardware, a fully functional impedance-sensing system with expanded bandwidth and higher transmission power could fit within a smartwatch-sized device. This capability is discussed further in Section 10.3.

10 DISCUSSION

Through our simulations, technical evaluations, and user evaluations, we demonstrated how Z-Band effectively integrates impedance and inertial sensing to enable precise and versatile touch interactions on everyday surfaces, overcoming the limitations of traditional input methods in XR environments. We now contextualize our work and related research, discuss the limitations of our current implementation, and highlight directions for future research. Finally, we explore the broader applications of Z-Band in real-world scenarios.

10.1 Applications

Z-Band demonstrates broad potential across XR, wearables, accessibility, and smart environments. Its unique capabilities enable several novel interaction paradigms.

Transforming Everyday Surfaces into Interactive Touch Interfaces. Z-Band redefines interaction by turning ordinary surfaces into touch-sensitive digital interfaces, enabling seamless, intuitive control of smart environments.

With this capability, users can interact with everyday objects—such as desks, tables, walls, or clothing—without needing dedicated touchscreens or physical buttons. In smart home environments, users can tap or swipe on tables to adjust lighting, control media playback, or modify thermostat settings, eliminating the need for remotes or voice commands. Walls and kitchen countertops can function as interactive hubs for managing smart appliances. In wearable and on-body interactions, Z-Band enables users to control devices by tapping or swiping on garments, such as sleeves or pant legs, for discreet media playback or call management. Similarly, one hand can interact with the palm or forearm to control AR/VR headsets or smartwatches without disrupting immersion. Z-Band can create more seamless and intuitive user experiences by integrating digital interactions into physical environments.

Enhance Accessibility Through Intentional Interaction Detection. Z-Band offers particular utility for users with motor control challenges through its precise pressure sensing capabilities. The system can effectively differentiate between intentional inputs and inadvertent contact by monitoring applied pressure, thereby filtering out unintended interactions caused by tremors or involuntary movements [5]. This aligns well with existing research [19] showing that users with motor control disabilities typically apply greater force during tapping interactions (6.2 N on average, compared to the standard 0.98 N activation threshold). Z-Band's S_{21} pressure sensitivity range accommodates these interaction patterns, enabling personalized pressure threshold calibration for individual users.

Context-Aware, Material-Based Interaction. During our exploration, we identified a unique capability of Z-Band: its ability to distinguish between different surfaces, such as copper versus wood. Figure 9c shows the raw data captured by the Z-Band prototype for different materials. This capability supports two key applications. First, it enhances security by restricting interactions to specific surfaces—for example, allowing input only on wooden furniture to prevent accidental activations elsewhere. Second, it enables context-aware functionality, where interactions adapt based on the material—tapping on wood could adjust ambient lighting while touching skin could trigger media playback controls. Future research will further explore and refine material differentiation to expand Z-Band's interactive potential.

10.2 Future Interactions

Multi-Finger and Hand-Specific Interactions. While Z-Band currently focuses on single-finger touch interactions, expanding to multi-finger and hand-specific interactions could enable richer and more expressive inputs. Distinguishing between different fingers interacting with a surface would permit gestures such as pinch-to-zoom, multi-finger scrolling, or chorded inputs similar to keyboard shortcuts. Future iterations could incorporate electrode arrays or machine learning models trained to recognize characteristic impedance changes caused by different fingers. Additionally, tracking impedance variations across the hand could enable differentiation between left and right hands, facilitating bi-manual interactions.

Beyond Touch Detection. Z-Band's sensing capabilities could be leveraged for a broader range of interactions, including proximity-based gestures and grip recognition. Since RF impedance is affected by hand proximity, the system could detect hovering gestures, enabling touch-free interactions with virtual interfaces. Grip and hand pose recognition could further extend its use in augmented reality (AR) and virtual reality (VR) applications, where natural hand-based interactions are essential.

10.3 Hardware Miniaturization and Optimization

The current Z-Band prototype is intentionally designed with a modular and large-form factor to prioritize ease of use, rapid prototyping, and streamlined debugging during user evaluation. By leveraging commercially available development boards, such as the LiteVNA and Raspberry Pi, we ensured reliability while minimizing debugging

overhead. These off-the-shelf components, having undergone rigorous testing before market release, allowed us to focus on refining Z-Band's sensing capabilities rather than dealing with hardware inconsistencies.

However, this prototype does not reflect the fundamental limitations of our approach. The large and modular design primarily facilitates experimental flexibility rather than defining the ultimate form factor of Z-Band. Future iterations will replace the Raspberry Pi and off-the-shelf VNA with custom-designed circuits optimized specifically for bio-impedance sensing. Prior work by Zhang et al. [60] indicates that only 15% of the NanoVNA's (comparable to LiteVNA) physical area is dedicated to actual impedance measurement circuitry, with the remaining space occupied by displays and power management components. This suggests that a significant reduction in device size is feasible without compromising performance.

Recent advancements in compact impedance measurement hardware, such as the ADL5960 chip-based VNA[4], offer promising opportunities for miniaturization. This highly integrated solution eliminates the need for bulky external components by incorporating a built-in local oscillator. Similarly, active circulator designs [45] significantly reduce hardware size compared to their passive counterparts, further contributing to a compact implementation.

Additionally, our final S_{21} through-path measurement design (Figure 9) eliminates the need for inductive components, enabling a simpler circuit layout. Unlike the earlier Coupler Reflectometry design (Figure 8), which relied on additional RF components, the optimized S_{21} -based architecture is well-suited for further miniaturization.

By integrating these improvements, Z-Band can evolve into a sleek, wrist-worn form factor without sacrificing functionality. These advancements pave the way for practical, real-world deployments, making Z-Band a viable sensing technology for next-generation wearable interfaces.

10.4 Battery Life and Future Improvements

Battery life is a key consideration for wearable devices. Our current Z-Band prototype, with its off-the-shelf components and continuous sensing, has limited battery life. However, we could significantly improve this in future iterations. One key strategy is *duty cycling*, where the system intelligently alternates between active sensing and sleep modes. We could drastically reduce power consumption by activating the sensors only when necessary, such as when the user is likely to interact with a surface. Duty cycling can be achieved through various techniques, including using the IMU to detect hand movements that suggest an impending interaction, employing proximity sensors to detect when the hand is near a surface, or even allowing the user to activate the sensing system manually, when needed. Additionally, utilizing lower-power components, such as a more efficient microcontroller and a custom-designed impedance analyzer, could further reduce power consumption. Finally, replacing WiFi with BLE for wireless communication or logging data locally and transmitting it in bursts instead of streaming could further conserve energy.

11 CONCLUSION

This research introduces Z-Band, a wearable device that enables interaction with everyday surfaces. By combining bio-impedance and inertial sensing, Z-Band offers robust and versatile touch detection, even on challenging dielectric materials. Our investigation spans theoretical foundations, simulation-based analysis, and the development of analog front-end architectures tailored for wrist-worn impedance sensing with VNAs. Through rigorous user evaluations, we demonstrate Z-Band's effectiveness in accurately recognizing a diverse set of gestures, including taps and swipes, even amidst the complexities of real-world scenarios. The system's ability to achieve high accuracy for touch detection without requiring per-user calibration underscores its potential for seamless integration into daily life. By enabling natural and intuitive touch interactions on everyday surfaces, Z-Band paves the way for a future where interactions seamlessly integrate the digital and physical realms.

[4] https://www.analog.com/adl5960.html

References

[1] Alan Bränzel, Christian Holz, Daniel Hoffmann, Dominik Schmidt, Marius Knaust, Patrick Lühne, René Meusel, Stephan Richter, and Patrick Baudisch. 2013. GravitySpace: tracking users and their poses in a smart room using a pressure-sensing floor. In Proceedings of the SIGCHI Conference on Human Factors in Computing Systems. 725–734.

[2] B. H. Brown, R. H. Smallwood, D. C. Barber, P. V. Lawford, and D. R. Hose. 2001. Measurement Science and Technology. Meas. Sci. Technol. 12, 10 (2001), 1744. doi:10.1088/0957-0233/12/10/703

[3] William A.S. Buxton. 1990. A three-state model of graphical input. In IFIP TC13 International Conference on Human-Computer Interaction. https://api.semanticscholar.org/CorpusID:36550963

[4] Jared Cechanowicz, Pourang Irani, and Sriram Subramanian. 2007. Augmenting the mouse with pressure sensitive input. In Proceedings of the SIGCHI Conference on Human Factors in Computing Systems (San Jose, California, USA) (CHI '07). Association for Computing Machinery, New York, NY, USA, 1385–1394. doi:10.1145/1240624.1240835

[5] Tingyu Cheng, Zhihan Zhang, Bingrui Zong, Yuhui Zhao, Zekun Chang, Yejun Kim, Clement Zheng, Gregory D. Abowd, and HyunJoo Oh. 2023. SwellSense: Creating 2.5D interactions with micro-capsule paper. In Proceedings of the 2023 CHI Conference on Human Factors in Computing Systems (New York, NY, USA, 2023-04-19) (CHI '23). Association for Computing Machinery, 1–13. doi:10.1145/3544548.3581125

[6] NanoVNA Developers Community. 2024. NanoVNA: Vector Network Analyzer. Available online at the NanoVNA official website. https://nanovna.com/ Accessed: 2024-09-08.

[7] CTRL-labs at Reality Labs, David Sussillo, Patrick Kaifosh, and Thomas Reardon. 2024. A generic noninvasive neuromotor interface for human-computer interaction. doi:10.1101/2024.02.23.581779 Pages: 2024.02.23.581779 Section: New Results.

[8] Paul Dietz and Darren Leigh. 2001. DiamondTouch: a multi-user touch technology. In Proceedings of the 14th annual ACM symposium on User interface software and technology (New York, NY, USA, 2001-11-11) (UIST '01). Association for Computing Machinery, 219–226. doi:10.1145/502348.502389

[9] Yuran Ding, Craig Shultz, and Chris Harrison. 2023. Surface I/O: Creating Devices with Functional Surface Geometry for Haptics and User Input. In Proceedings of the 2023 CHI Conference on Human Factors in Computing Systems (Hamburg, Germany) (CHI '23). Association for Computing Machinery, New York, NY, USA, Article 423, 22 pages. doi:10.1145/3544548.3581037

[10] I. Dove. 2014. Analysis of Radio Propagation Inside the Human Body for in-Body Localization Purposes. http://essay.utwente.nl/66071/

[11] Eleshop. 2023. LiteVNA User Guide. https://static.eleshop.nl/mage/media/downloads/LiteVNA_User-Guide.pdf Accessed: September 9, 2024.

[12] Nicholas D. Everett. 2019. Instantaneous Bandwidth Expansion Using Software Defined Radios. https://scholar.afit.edu/etd/2255 Accessed: 2024-09-08.

[13] Jun Gong, Aakar Gupta, and Hrvoje Benko. 2020. Acustico: Surface Tap Detection and Localization using Wrist-based Acoustic TDOA Sensing. In Proceedings of the 33rd Annual ACM Symposium on User Interface Software and Technology (New York, NY, USA, 2020-10-20) (UIST '20). Association for Computing Machinery, 406–419. doi:10.1145/3379337.3415901

[14] Tobias Grosse-Puppendahl, Christian Holz, Gabe Cohn, Raphael Wimmer, Oskar Bechtold, Steve Hodges, Matthew S. Reynolds, and Joshua R. Smith. 2017. Finding Common Ground: A Survey of Capacitive Sensing in Human-Computer Interaction. In Proceedings of the 2017 CHI Conference on Human Factors in Computing Systems (Denver, Colorado, USA) (CHI '17). Association for Computing Machinery, New York, NY, USA, 3293–3315. doi:10.1145/3025453.3025808

[15] Yizheng Gu, Chun Yu, Zhipeng Li, Weiqi Li, Shuchang Xu, Xiaoying Wei, and Yuanchun Shi. 2019. Accurate and Low-Latency Sensing of Touch Contact on Any Surface with Finger-Worn IMU Sensor. In Proceedings of the 32nd Annual ACM Symposium on User Interface Software and Technology (New Orleans, LA, USA) (UIST '19). Association for Computing Machinery, New York, NY, USA, 1059–1070. doi:10.1145/3332165.3347947

[16] Chris Harrison and Scott E Hudson. 2008. Scratch input: creating large, inexpensive, unpowered and mobile finger input surfaces. In Proceedings of the 21st annual ACM symposium on User interface software and technology. 205–208.

[17] Chris Harrison, Desney Tan, and Dan Morris. 2010. Skinput: appropriating the body as an input surface. In Proceedings of the SIGCHI Conference on Human Factors in Computing Systems (New York, NY, USA, 2010-04-10) (CHI '10). Association for Computing Machinery, 453–462. doi:10.1145/1753326.1753394

[18] Yasha Iravantchi, Yi Zhao, Kenrick Kin, and Alanson P Sample. 2023. SAWSense: Using Surface Acoustic Waves for Surface-bound Event Recognition. In Proceedings of the 2023 CHI Conference on Human Factors in Computing Systems. 1–18.

[19] Curt B. Irwin and Mary E. Sesto. 2012. Performance and touch characteristics of disabled and non-disabled participants during a reciprocal tapping task using touch screen technology. 43, 6 (2012), 1038–1043. doi:10.1016/j.apergo.2012.03.003

[20] Peiqi Kang, Jinxuan Li, Bingfei Fan, Shuo Jiang, and Peter Shull. 2021. Wrist-Worn Hand Gesture Recognition While Walking via Transfer Learning. IEEE Journal of Biomedical and Health Informatics PP (07 2021), 1–1. doi:10.1109/JBHI.2021.3100099

[21] Wolf Kienzle, Eric Whitmire, Chris Rittaler, and Hrvoje Benko. 2021. ElectroRing: Subtle Pinch and Touch Detection with a Ring. In Proceedings of the 2021 CHI Conference on Human Factors in Computing Systems (New York, NY, USA, 2021-05-07) (CHI '21).

Association for Computing Machinery, 1–12. doi:10.1145/3411764.3445094
[22] Daehwa Kim and Chris Harrison. 2022. EtherPose: Continuous Hand Pose Tracking with Wrist-Worn Antenna Impedance Characteristic Sensing. In Proceedings of the 35th Annual ACM Symposium on User Interface Software and Technology (New York, NY, USA, 2022-10-28) (UIST '22). Association for Computing Machinery, 1–12. doi:10.1145/3526113.3545665
[23] Daehwa Kim and Chris Harrison. 2023. Pantœnna: Mouth pose estimation for ar/vr headsets using low-profile antenna and impedance characteristic sensing. In Proceedings of the 36th Annual ACM Symposium on User Interface Software and Technology (New York, NY, USA, 2023-10-29) (UIST '23). Association for Computing Machinery, 1–12. doi:10.1145/3586183.3606805
[24] Daehwa Kim and Chris Harrison. 2023. Pantoenna: Mouth pose estimation for ar/vr headsets using low-profile antenna and impedance characteristic sensing. In Proceedings of the 36th Annual ACM Symposium on User Interface Software and Technology (San Francisco, CA, USA) (UIST '23). Association for Computing Machinery, New York, NY, USA, Article 83, 12 pages. doi:10.1145/3586183.3606805
[25] Daehwa Kim, Eric Whitmire, Roger Boldu, Wolf Kienzle, and Hrvoje Benko. 2024. SoundScroll: Robust Finger Slide Detection Using Friction Sound and Wrist-Worn Microphones. In Proceedings of the 2024 ACM International Symposium on Wearable Computers (New York, NY, USA, 2024-10-05) (ISWC '24). Association for Computing Machinery. doi:10.1145/3675095.3676614
[26] Kwangsoo Kim, Mi-Hee Lee, Jungchae Kim, Seok Jung, Sun Jee, and Sun kyung Yoo. 2009. Performance evaluation of the electrode configuration in bioelectrical impedance analysis for visceral fat measurement. Conference proceedings : ... Annual International Conference of the IEEE Engineering in Medicine and Biology Society. IEEE Engineering in Medicine and Biology Society. Conference 2009 (09 2009), 892–5. doi:10.1109/IEMBS.2009.5335377
[27] Alexander Kyu, Hongyu Mao, Junyi Zhu, Mayank Goel, and Karan Ahuja. 2024. EITPose: Wearable and Practical Electrical Impedance Tomography for Continuous Hand Pose Estimation. In Proceedings of the CHI Conference on Human Factors in Computing Systems (New York, NY, USA, 2024-05-11) (CHI '24). Association for Computing Machinery, 1–10. doi:10.1145/3613904.3642663
[28] Gierad Laput, Robert Xiao, and Chris Harrison. 2016. ViBand: High-Fidelity Bio-Acoustic Sensing Using Commodity Smartwatch Accelerometers. In Proceedings of the 29th Annual Symposium on User Interface Software and Technology (New York, NY, USA, 2016-10-16) (UIST '16). Association for Computing Machinery, 321–333. doi:10.1145/2984511.2984582
[29] Eric Larson, Gabe Cohn, Sidhant Gupta, Xiaofeng Ren, Beverly Harrison, Dieter Fox, and Shwetak Patel. 2011. HeatWave: thermal imaging for surface user interaction. In Proceedings of the SIGCHI Conference on Human Factors in Computing Systems (New York, NY, USA, 2011-05-07) (CHI '11). Association for Computing Machinery, 2565–2574. doi:10.1145/1978942.1979317
[30] Chen Liang, Xutong Wang, Zisu Li, Chi Hsia, Mingming Fan, Chun Yu, and Yuanchun Shi. 2023. ShadowTouch: Enabling Free-Form Touch-Based Hand-to-Surface Interaction with Wrist-Mounted Illuminant by Shadow Projection. In Proceedings of the 36th Annual ACM Symposium on User Interface Software and Technology (San Francisco, CA, USA) (UIST '23). Association for Computing Machinery, New York, NY, USA, Article 27, 14 pages. doi:10.1145/3586183.3606785
[31] Robert W. Lindeman, John L. Sibert, and James K. Hahn. 1999. Towards usable VR: an empirical study of user interfaces for immersive virtual environments. In Proceedings of the SIGCHI conference on Human Factors in Computing Systems (New York, NY, USA, 1999-05-01) (CHI '99). Association for Computing Machinery, 64–71. doi:10.1145/302979.302995
[32] Yilin Liu, Shijia Zhang, and Mahanth Gowda. 2021. NeuroPose: 3D Hand Pose Tracking using EMG Wearables. In Proceedings of the Web Conference 2021 (New York, NY, USA, 2021-06-03) (WWW '21). Association for Computing Machinery, 1471–1482. doi:10.1145/3442381.3449890
[33] S. Mansouri, Yousef Alharbi, Fatma Haddad, Souhir Chabcoub, Anwar Alshrouf, and Amr A. Abd-Elghany. 2021. Electrical Impedance Tomography – Recent Applications and Developments. Journal of Electrical Bioimpedance (2021). doi:10.2478/joeb-2021-0007
[34] Ørjan G. Martinsen and Arto Heiskanen. 2023. Bioimpedance and Bioelectricity Basics, Fourth Edition (4th ed.). Elsevier, United Kingdom. doi:10.1016/C2018-0-04808-2
[35] Manuel Meier, Paul Streli, Andreas Fender, and Christian Holz. 2021. TapID: Rapid Touch Interaction in Virtual Reality using Wearable Sensing. In 2021 IEEE Virtual Reality and 3D User Interfaces (VR). 519–528. doi:10.1109/VR50410.2021.00076
[36] Vimal Mollyn and Chris Harrison. 2024. EgoTouch: On-Body Touch Input Using AR/VR Headset Cameras. In Proceedings of the 37th Annual ACM Symposium on User Interface Software and Technology (Pittsburgh, PA, USA) (UIST '24). Association for Computing Machinery, New York, NY, USA, Article 69, 11 pages. doi:10.1145/3654777.3676455
[37] Takehiro Niikura, Yoshihiro Watanabe, and Masatoshi Ishikawa. 2014. Anywhere surface touch: utilizing any surface as an input area. In Proceedings of the 5th Augmented Human International Conference (New York, NY, USA, 2014-03-07) (AH '14). Association for Computing Machinery, 1–8. doi:10.1145/2582051.2582090
[38] T. Scott Saponas, Desney S. Tan, Dan Morris, Ravin Balakrishnan, Jim Turner, and James A. Landay. 2009. Enabling always-available input with muscle-computer interfaces. In Proceedings of the 22nd annual ACM symposium on User interface software and technology (New York, NY, USA, 2009-10-04) (UIST '09). Association for Computing Machinery, 167–176. doi:10.1145/1622176.1622208
[39] Munehiko Sato, Ivan Poupyrev, and Chris Harrison. 2012. Touché: enhancing touch interaction on humans, screens, liquids, and everyday objects. In Proceedings of the SIGCHI Conference on Human Factors in Computing Systems (Austin Texas USA, 2012-05-05). ACM, 483–492. doi:10.1145/2207676.2207743

[40] Jin Keun Seo and Eung Je Woo. 2014. Electrical Tissue Property Imaging at Low Frequency Using MREIT. IEEE Transactions on Biomedical Engineering 61, 5 (2014), 1390–1399. doi:10.1109/TBME.2014.2298859

[41] Yilei Shi, Haimo Zhang, Kaixing Zhao, Jiashuo Cao, Mengmeng Sun, and Suranga Nanayakkara. 2020. Ready, Steady, Touch! Sensing Physical Contact with a Finger-Mounted IMU. 4, 2 (2020), 59:1–59:25. doi:10.1145/3397309

[42] Chapa Sirithunge, Huijiang Wang, and Fumiya Iida. 2024. Soft touchless sensors and touchless sensing for soft robots. Frontiers in Robotics and AI 11 (2024). doi:10.3389/frobt.2024.1224216

[43] Alexander Stahn, Elmarie Terblanche, and Hanns-Christian Gunga. 2012. Use of Bioelectrical Impedance: General Principles and Overview. Springer New York, New York, NY, 49–90. doi:10.1007/978-1-4419-1788-1_3

[44] Craig Stewart, Michael Rohs, Sven Kratz, and Georg Essl. 2010. Characteristics of pressure-based input for mobile devices. In Proceedings of the SIGCHI Conference on Human Factors in Computing Systems (Atlanta, Georgia, USA) (CHI '10). Association for Computing Machinery, New York, NY, USA, 801–810. doi:10.1145/1753326.1753444

[45] SV3ORA. [n. d.]. A low frequency circulator/isolator for lab measurements and signal routing by SV3ORA. http://qrp.gr/circulator/index.htm

[46] Keysight Technologies. 2024. E4991B Impedance Analyzer, 1 MHz - 500 MHz, 1 GHz, 3 GHz. https://www.keysight.com/us/en/product/E4991B/impedance-analyzer-1-mhz-500-mhz-1-ghz-3-ghz.html Accessed: 2024-09-08.

[47] Anandghan Waghmare, Youssef Ben Taleb, Ishan Chatterjee, Arjun Narendra, and Shwetak Patel. 2023. Z-Ring: Single-Point Bio-Impedance Sensing for Gesture, Touch, Object and User Recognition. In Proceedings of the 2023 CHI Conference on Human Factors in Computing Systems (Hamburg, Germany) (CHI '23). Association for Computing Machinery, New York, NY, USA, Article 150, 18 pages. doi:10.1145/3544548.3581422

[48] Anandghan Waghmare, Ishan Chatterjee, and Shwetak Patel. 2023. Z-Pose: Continuous 3D Hand Pose Tracking Using Single-Point Bio-Impedance Sensing on a Ring. In Proceedings of the 2nd Workshop on Smart Wearable Systems and Applications. 1–6.

[49] Nana Wang, Jianwei Niu, Xuefeng Liu, Dongqin Yu, Guogang Zhu, Xinghao Wu, Mingliang Xu, and Hao Su. 2024. BeyondVision: An EMG-driven Micro Hand Gesture Recognition Based on Dynamic Segmentation, Vol. 7. 6044–6052. doi:10.24963/ijcai.2024/668 ISSN: 1045-0823.

[50] Yuntao Wang, Chun Yu, Lin Du, Jin Huang, and Yuanchun Shi. 2014. BodyRC: Exploring Interaction Modalities Using Human Body as Lossy Signal Transmission Medium. In Proceedings of the 2014 IEEE 11th Intl Conf on Ubiquitous Intelligence and Computing and 2014 IEEE 11th Intl Conf on Autonomic and Trusted Computing and 2014 IEEE 14th Intl Conf on Scalable Computing and Communications and Its Associated Workshops (UIC-ATC-ScalCom) (USA, 2014-12-09) (UIC-ATC-SCALCOM '14). IEEE Computer Society, 260–267. doi:10.1109/UIC-ATC-ScalCom.2014.73

[51] Ziyi Xia, Xincheng Huang, Sidney S Fels, and Robert Xiao. 2025. HaloTouch: Using IR Multi-Path Interference to Support Touch Interactions with General Surfaces. In Proceedings of the 2025 CHI Conference on Human Factors in Computing Systems (CHI '25). Association for Computing Machinery, New York, NY, USA, Article 548, 17 pages. doi:10.1145/3706598.3714179

[52] Robert Xiao, Scott Hudson, and Chris Harrison. 2016. DIRECT: Making Touch Tracking on Ordinary Surfaces Practical with Hybrid Depth-Infrared Sensing. In Proceedings of the 2016 ACM International Conference on Interactive Surfaces and Spaces (New York, NY, USA, 2016-11-06) (ISS '16). Association for Computing Machinery, 85–94. doi:10.1145/2992154.2992173

[53] Xing-Dong Yang, Tovi Grossman, Daniel Wigdor, and George Fitzmaurice. 2012. Magic finger: always-available input through finger instrumentation. In Proceedings of the 25th annual ACM symposium on User interface software and technology. 147–156.

[54] Yang Zhang and Chris Harrison. 2015. Tomo: Wearable, Low-Cost Electrical Impedance Tomography for Hand Gesture Recognition. In Proceedings of the 28th Annual ACM Symposium on User Interface Software & Technology (New York, NY, USA, 2015-11-05) (UIST '15). Association for Computing Machinery, 167–173. doi:10.1145/2807442.2807480

[55] Yang Zhang, Wolf Kienzle, Yanjun Ma, Shiu S. Ng, Hrvoje Benko, and Chris Harrison. 2019. ActiTouch: Robust Touch Detection for On-Skin AR/VR Interfaces. In Proceedings of the 32nd Annual ACM Symposium on User Interface Software and Technology (New York, NY, USA, 2019-10-17) (UIST '19). Association for Computing Machinery, 1151–1159. doi:10.1145/3332165.3347869

[56] Yang Zhang, Gierad Laput, and Chris Harrison. 2017. Electrick: Low-Cost Touch Sensing Using Electric Field Tomography. In Proceedings of the 2017 CHI Conference on Human Factors in Computing Systems (New York, NY, USA, 2017-05-02) (CHI '17). Association for Computing Machinery, 1–14. doi:10.1145/3025453.3025842

[57] Yang Zhang, Robert Xiao, and Chris Harrison. 2016. Advancing Hand Gesture Recognition with High Resolution Electrical Impedance Tomography. In Proceedings of the 29th Annual Symposium on User Interface Software and Technology (New York, NY, USA, 2016-10-16) (UIST '16). Association for Computing Machinery, 843–850. doi:10.1145/2984511.2984574

[58] Yang Zhang, Chouchang Yang, Scott E Hudson, Chris Harrison, and Alanson Sample. 2018. Wall++ room-scale interactive and context-aware sensing. In Proceedings of the 2018 chi conference on human factors in computing systems. 1–15.

[59] Yang Zhang, Junhan Zhou, Gierad Laput, and Chris Harrison. 2016. SkinTrack: Using the Body as an Electrical Waveguide for Continuous Finger Tracking on the Skin. In Proceedings of the 2016 CHI Conference on Human Factors in Computing Systems (San Jose, California, USA) (CHI '16). Association for Computing Machinery, New York, NY, USA, 1491–1503. doi:10.1145/2858036.2858082

[60] Zhihan Zhang, Mallory Parker, Kuotian Liao, Jerry Cao, Anandghan Waghmare, Joseph Breda, Chris Matsumura, Serena Eley, Eleftheria Roumeli, Shwetak Patel, and Vikram Iyer. 2024. Biodegradable Interactive Materials. doi:10.48550/arXiv.2404.03130 arXiv:2404.03130 [cs].

[61] Jian Feng Zhao, Xi Mei Chen, Bo Dong Liang, and Qiu Xia Chen. 2017. A Review on Human Body Communication: Signal Propagation Model, Communication Performance, and Experimental Issues. Wireless Communications and Mobile Computing 2017, 1 (2017), 5842310. doi:10.1155/2017/5842310 arXiv:https://onlinelibrary.wiley.com/doi/pdf/10.1155/2017/5842310

[62] Junyi Zhu, Jackson C Snowden, Joshua Verdejo, Emily Chen, Paul Zhang, Hamid Ghaednia, Joseph H Schwab, and Stefanie Mueller. 2021. EIT-kit: An Electrical Impedance Tomography Toolkit for Health and Motion Sensing. In The 34th Annual ACM Symposium on User Interface Software and Technology (New York, NY, USA, 2021-10-12) (UIST '21). Association for Computing Machinery, 400–413. doi:10.1145/3472749.3474758

[63] T. G. Zimmerman. 1996. Personal Area Networks: Near-field intrabody communication. IBM Systems Journal 35, 3.4 (1996), 609–617. doi:10.1147/sj.353.0609